



Temporal Evolution of the High-energy Irradiation and Water Content of TRAPPIST-1 Exoplanets

V. Bourrier¹ , J. de Wit² , E. Bolmont³, V. Stamenković^{4,5} , P. J. Wheatley⁶ , A. J. Burgasser⁷ , L. Delrez⁸,
B.-O. Demory⁹ , D. Ehrenreich¹ , M. Gillon¹⁰ , E. Jehin¹⁰, J. Leconte¹¹, S. M. Lederer¹², N. Lewis¹³ ,
A. H. M. J. Triaud¹⁴ , and V. Van Grootel¹⁰

¹ Observatoire de l'Université de Genève, 51 chemin des Maillettes, 1290 Sauverny, Switzerland

² Department of Earth, Atmospheric and Planetary Sciences, Massachusetts Institute of Technology, 77 Massachusetts Avenue, Cambridge, MA 02139, USA

³ Laboratoire AIM Paris-Saclay, CEA/DRF—CNRS—Univ. Paris Diderot—IRFU/SAP, Centre de Saclay, F-91191 Gif-sur-Yvette Cedex, France

⁴ Division of Geological and Planetary Sciences, California Institute of Technology, Pasadena, CA 91125, USA

⁵ Jet Propulsion Laboratory, California Institute of Technology, Pasadena, CA 91109 USA

⁶ Department of Physics, University of Warwick, Coventry CV4 7AL, UK

⁷ Center for Astrophysics and Space Science, University of California San Diego, La Jolla, CA 92093, USA

⁸ Cavendish Laboratory, J J Thomson Avenue, Cambridge, CB3 0HE, UK

⁹ University of Bern, Center for Space and Habitability, Sidlerstrasse 5, CH-3012, Bern, Switzerland

¹⁰ Institut d'Astrophysique et de Géophysique, Université de Liège, Allée du 6 Aout 19C, B-4000 Liège, Belgium

¹¹ Laboratoire d'Astrophysique de Bordeaux, Univ. Bordeaux, CNRS, B18N, allée Geoffroy Saint-Hilaire, F-33615 Pessac, France

¹² NASA Johnson Space Center, 2101 NASA Parkway, Houston, Texas, 77058, USA

¹³ Space Telescope Science Institute, 3700 San Martin Drive, Baltimore, Maryland 21218, USA

¹⁴ Institute of Astronomy, Madingley Road, Cambridge CB3 0HA, UK

Received 2017 May 21; revised 2017 July 19; accepted 2017 July 27; published 2017 August 31

Abstract

The ultracool dwarf star TRAPPIST-1 hosts seven Earth-size transiting planets, some of which could harbor liquid water on their surfaces. Ultraviolet observations are essential to measuring their high-energy irradiation and searching for photodissociated water escaping from their putative atmospheres. Our new observations of the TRAPPIST-1 Ly α line during the transit of TRAPPIST-1c show an evolution of the star emission over three months, preventing us from assessing the presence of an extended hydrogen exosphere. Based on the current knowledge of the stellar irradiation, we investigated the likely history of water loss in the system. Planets b to d might still be in a runaway phase, and planets within the orbit of TRAPPIST-1g could have lost more than 20 Earth oceans after 8 Gyr of hydrodynamic escape. However, TRAPPIST-1e to h might have lost less than three Earth oceans if hydrodynamic escape stopped once they entered the habitable zone (HZ). We caution that these estimates remain limited by the large uncertainty on the planet masses. They likely represent upper limits on the actual water loss because our assumptions maximize the X-rays to ultraviolet-driven escape, while photodissociation in the upper atmospheres should be the limiting process. Late-stage outgassing could also have contributed significant amounts of water for the outer, more massive planets after they entered the HZ. While our results suggest that the outer planets are the best candidates to search for water with the *JWST*, they also highlight the need for theoretical studies and complementary observations in all wavelength domains to determine the nature of the TRAPPIST-1 planets and their potential habitability.

Key words: planetary systems – planets and satellites: atmospheres – planets and satellites: terrestrial planets – stars: individual (TRAPPIST-1) – stars: low-mass – ultraviolet: planetary systems

1. Introduction

The TRAPPIST-1 system has been found to host an unprecedented seven Earth-sized planets (Gillon et al. 2016, 2017). All seven of the TRAPPIST-1 planets were detected using the transit method (Winn 2010), which allows for the direct determination of their radii (Gillon et al. 2017, Table 1). Masses for the TRAPPIST-1 planets (Gillon et al. 2017, Table 1) were derived through transit-timing variations (TTV; Holman & Murray 2005). The seventh planet's properties were recently refined by Luger et al. (2017), who showed that three-body resonances link every planet of this complex system. The combined mass and radius measurements for the TRAPPIST-1 planets are consistent with rocky, water-enriched bulk compositions, with TRAPPIST-1f having a density low enough to harbor up to 50% of water in its mass. Three of the TRAPPIST-1 planets (e to g) orbit within the habitable zone (HZ; e.g., Kopparapu 2013), where water on a planet's surface is more likely to be in a liquid state. The planets in the

TRAPPIST-1 system present a unique opportunity for single-system comparative studies aimed at understanding the formation and evolution of terrestrial exoplanet atmospheres.

The atmospheres of terrestrial exoplanets are expected to be diverse and shaped by a number of physical processes (e.g., Leconte et al. 2015). Observationally probing the TRAPPIST-1 planets over a broad wavelength range from the ultraviolet (UV) to the infrared (IR) provides insights into their current state and the dominant physical processes shaping their atmospheres. Because the TRAPPIST-1 planets transit their host stars as seen from Earth, their atmospheres can be probed via transmission spectroscopy (e.g., Seager & Sasselov 2000; Kaltenegger & Traub 2009). The atmospheres of TRAPPIST-1b and c were probed at IR wavelengths by de Wit et al. (2016) using the *Hubble Space Telescope* (*HST*), which found the atmospheres of these planets to be inconsistent with clear, hydrogen-rich “primordial” atmospheres. However, a number of plausible scenarios still exist for the atmospheres of TRAPPIST-1b and c, including water-rich and aerosol-laden

Table 1
Characteristics of the TRAPPIST-1 Exoplanets

Planets	b	c	d	e	f	g	h
$M_p (M_\oplus)$	0.85 ± 0.72	1.38 ± 0.61	0.41 ± 0.27	0.62 ± 0.58	0.68 ± 0.18	1.34 ± 0.88	$0.06\text{--}0.86$
$R_p (R_\oplus)$	1.086	1.056	0.772	0.918	1.045	1.127	0.752
$\rho_p (\rho_\oplus)$	0.66 ± 0.56	1.17 ± 0.53	0.89 ± 0.60	0.80 ± 0.76	0.60 ± 0.17	0.94 ± 0.63	$0.14\text{--}2.02$
a_p (au)	0.01111	0.01521	0.02144	0.02817	0.0371	0.0451	0.059

Notes. Note that the mass of planet h could not be determined with TTV, so we computed the mass range for two extreme compositions: 100% ice and 100% iron. We chose to base our analysis on the masses derived by Gillon et al. (2017) rather than those of Wang et al. (2017) and Quarles et al. (2017), because these latter works were still under review at the time of submission of this paper.

atmospheres. A robust interpretation of current and future observations of TRAPPIST-1 at IR wavelengths will require a better understanding of atmospheric chemistry and escape processes shaping these planets, which can be provided by observations at UV wavelengths.

Ultraviolet transit spectroscopy is a powerful way to search for signatures of atmospheric escape from exoplanets. Extended atmospheres of neutral hydrogen have been detected through observations of the stellar Lyman- α line ($\text{Ly}\alpha$) during the transit of Jupiter-mass planets (Vidal-Madjar et al. 2003; Lecavelier des Etangs et al. 2010, 2012; Ehrenreich et al. 2012) and Neptune-mass planets (Kulow et al. 2014; Ehrenreich et al. 2015). Because of their spatial extent and kinetic broadening (e.g., Ekenbäck et al. 2010; Bourrier & Lecavelier des Etangs 2013), exospheres transit longer than the lower atmospheric layers probed at optical and infrared wavelengths and yield deep transit signatures over a large spectral range. The case of the warm Neptune GJ 436b, in particular, revealed that small planets around cool M dwarfs can support giant exospheres, yielding up to half-eclipses of the star at $\text{Ly}\alpha$ (Bourrier et al. 2015, 2016b). UV observations of Earth-size planets in a system like TRAPPIST-1 thus offer great perspectives for constraining their atmospheric properties. The faint $\text{Ly}\alpha$ line of this cold M8 star was detected by Bourrier et al. 2017 (hereafter B17) using the *HST*, with enough light to perform transit spectroscopy. Hints of variations were identified at the time of the transits of inner planets b and c, which could either indicate extended atmospheres of neutral hydrogen or intrinsic stellar variability. The first objective of the present study was to reobserve the TRAPPIST-1 system in the $\text{Ly}\alpha$ line during a TRAPPIST-1c transit, to search for signatures of an extended atmosphere and to improve our understanding of the high-energy stellar emission.

Despite recent efforts (France et al. 2013, 2016), our understanding of the atmospheres of exoplanets around M dwarf stars remains limited by the lack of observational and theoretical knowledge about the UV and X-ray spectra of these cool stars. Yet these stars currently offer the best opportunity to detect and characterize Earth-size planets in the HZ. Measuring their UV irradiation is crucial because it affects the stability and erosion of planetary atmospheres (e.g., Lammer et al. 2003; Koskinen et al. 2007; Bolmont et al. 2017), controls photochemical reactions in the outer atmosphere (Miguel et al. 2015), and can further influence the development and survival of life on a planet surface (see, e.g., O’Malley-James & Kaltenegger 2017; Ranjan et al. 2017 for TRAPPIST-1). The high present-day X-ray to ultraviolet (XUV) emission from TRAPPIST-1 (Wheatley et al. 2017) and the fact that M dwarfs can remain active for several billion years suggest that the

atmospheres of the TRAPPIST-1 planets could have been subjected to significant mass loss over the course of their history. Water, in particular, could have been lost through photolysis and atmospheric escape, a process that has been previously studied by Bolmont et al. (2017) for TRAPPIST-1b, c, and d. At the time of their study, only those three planets were known, and the XUV emission of the star was not yet observationally constrained.

Our second objective in this paper is to revise the calculations of water loss for all TRAPPIST-1 planets, benefiting from our improved knowledge of the system architecture (Gillon et al. 2017) and of the stellar XUV irradiation (Wheatley et al. 2017, B17, and new $\text{Ly}\alpha$ measurements presented in this paper). The planet properties used in our analysis are given in Table 1. *HST* observations of TRAPPIST-1 are presented in Section 2 and used in Section 3 to study the high-energy stellar emission and its temporal evolution. Section 4 describes how the stellar irradiation influences the water loss from the planetary atmospheres, while Section 5 addresses the limiting effect of hydrogen production. We discuss the evolution of TRAPPIST-1 exoplanet atmospheres in Section 6.

2. Observations and Data Reduction

We observed the H I $\text{Ly}\alpha$ line (1215.6702 Å) of TRAPPIST-1 at four independent epochs in 2016, using the Space Telescope Imaging Spectrograph (STIS) instrument on board the *HST*. The log of these observations is given in Table 2. The star was observed at three epochs during Mid-Cycle Program 14493 (PI: V. Bourrier). Two consecutive *HST* orbits were obtained on 26 September (Visit 1), at a time when none of the seven planets were transiting (all planets were between 135° and 330° past their last respective transits). A single *HST* orbit was obtained during the transit of TRAPPIST-1b on 30 September (Visit 2), and another one about 1.7 hr after the transit of TRAPPIST-1c on 23 November (Visit 3). No other planets were close to transiting during Visits 2 and 3. The results of this reconnaissance program were published in B17. We obtained five new orbits on 2016 December 25 during the GO/DD Program 14900 (PI: J. de Wit). Visit 4 was scheduled to include a TRAPPIST-1c transit, to search for the signature of a hydrogen exosphere around the planet. The configuration of the planetary system at the time of Visit 4 is shown in Figure 1. Note that because of occultations by the Earth and the time required to acquire the target star with the *HST*, about one-third of an *HST* orbit could be spent observing TRAPPIST-1 at $\text{Ly}\alpha$.

All four visits made use of the STIS Far Ultraviolet Multi-Anode Microchannel Array (FUV-MAMA) detector and the G140M grating at 1222 Å. The data were reduced with the

Table 2
Log of TRAPPIST-1 Ly α Observations in 2016

Visit	Date	Time (UT)	
		Start	End
1	Sep 26	02:51:50	04:59:45
2	Sep 30	22:55:05	23:27:38
3	Nov 23	20:56:10	21:28:35
4	Dec 25	03:17:58	10:10:17

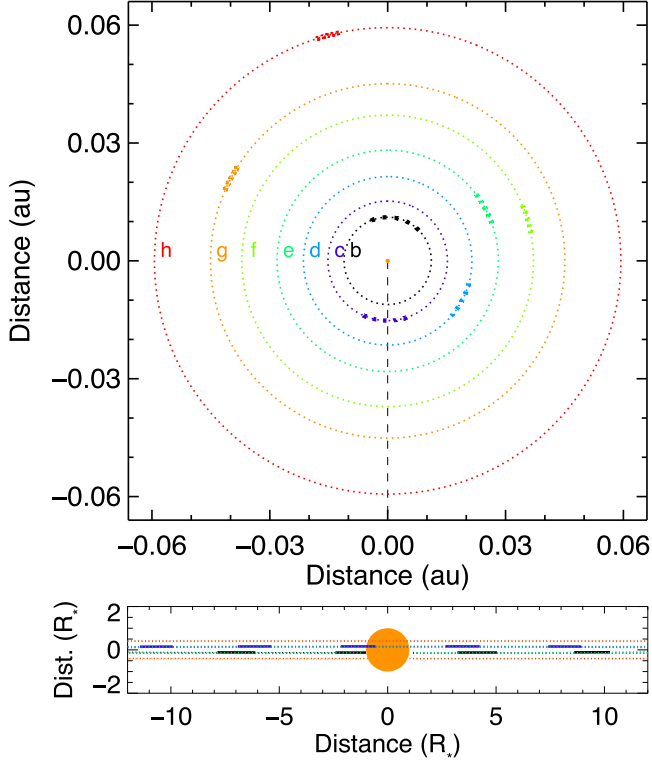


Figure 1. Orbital positions of the TRAPPIST-1 planets at the time of the *HST* observations in Visit 4. Each rectangle corresponds to the space covered by a planet during one of the *HST* orbits. Upper panel: view from above the planetary system. Planets are moving counterclockwise. The dashed black line indicates the line of sight (LOS) toward Earth. Star and orbital trajectories have the correct relative scale. Lower panel: view from Earth.

CALSTIS pipeline. In the region of the Ly α line, the background is dominated by the Earth’s geocoronal air glow emission (Vidal-Madjar et al. 2003). The error bars in the final 1D spectra account for the uncertainty in the air glow flux, but the correction performed by the pipeline can yield spurious flux values where the air glow is much stronger than the stellar line. The position, amplitude, and width of the air glow line profile varies in strength and position with the epoch of observation (e.g., Bourrier et al. 2016a), and we thus excluded from our analysis the contaminated ranges $[-3; 129] \text{ km s}^{-1}$ (Visit 1), $[-4; 102] \text{ km s}^{-1}$ (Visit 2), $[-8; 110] \text{ km s}^{-1}$ (Visit 3), and $[-29; 116] \text{ km s}^{-1}$ (Visit 4), defined in the star rest frame. The air glow is much stronger in Visit 4 because TRAPPIST-1 was nearly four months past opposition (see Figure 2), and we found that the stellar spectrum between -150 and -29 km s^{-1} depended on the areas of the 2D images used to build the background profile. The background is extracted and averaged automatically by the pipeline from two regions above and below the spectrum. For the FUV-MAMA D1 aperture used in Visit 4, the standard regions are five pixels wide and located

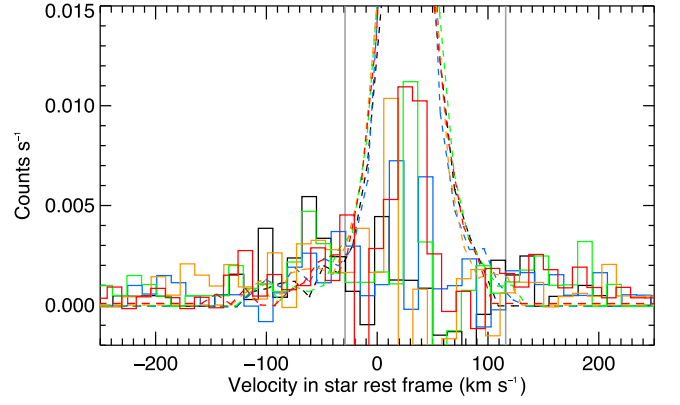


Figure 2. Raw spectra of the stellar Ly α line in Visit 4 (solid-line histogram), after correction from the geocoronal emission line (superimposed as a dashed line). Colors correspond to *HST* orbits at consecutive orbital phases (increasing from black to blue, green, orange, and red). Gray vertical lines indicate the range excluded from our analysis, where the air glow is so strong that its correction results in spurious flux values.

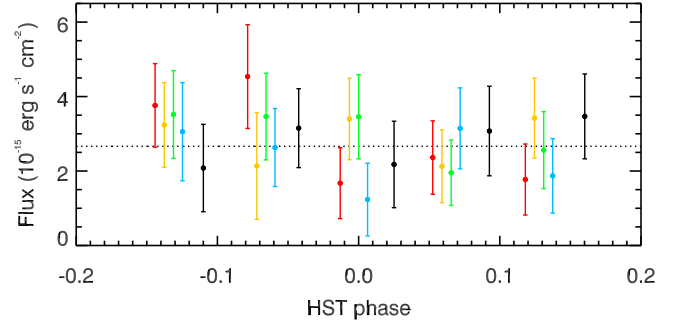


Figure 3. Ly α fluxes for all subexposures in Visit 4, integrated over the entire line (excluding the air glow range) and phase-folded on the *HST* orbital period. No variations caused by the telescope breathing were detected, with no significant deviations from the mean flux (black dashed line). Colors correspond to *HST* orbits at consecutive orbital phases (increasing from black to blue, green, orange, and red).

± 30 pixels from the spectrum along the cross-dispersion axis. We varied this distance and found that individual air-glow-corrected exposures showed differences in the blue wing of the stellar Ly α line when the background was extracted from regions farther than ~ 25 pixels from the spectrum. We thus limited the effect of air glow contamination by measuring an accurate local background within extraction regions that extend between six and 20 pixels from each side of the spectrum.

Data in each orbit, obtained in time-tagged mode, were divided into five shorter subexposures (varying from 380 to 450 s depending on the duration of the initial exposure). This allowed us to check for variations at short timescales within a given *HST* orbit caused by the telescope breathing (e.g., Bourrier et al. 2013). We modeled the breathing effect using either a Fourier series decomposition (Bourrier et al. 2016a) or a polynomial function (e.g., Ehrenreich et al. 2012). The model was fitted to the flux integrated over the entire Ly α line, excluding the range contaminated by air glow emission and using the Bayesian information criterion as a merit function (Crossfield et al. 2012). No variations caused by the telescope breathing were detected in any of the visits (see Figure 3 for Visit 4), most likely because it is dominated by the photon noise from the very faint Ly α line and because there are not enough *HST* orbits to sample its variations properly in Visits 1–3.

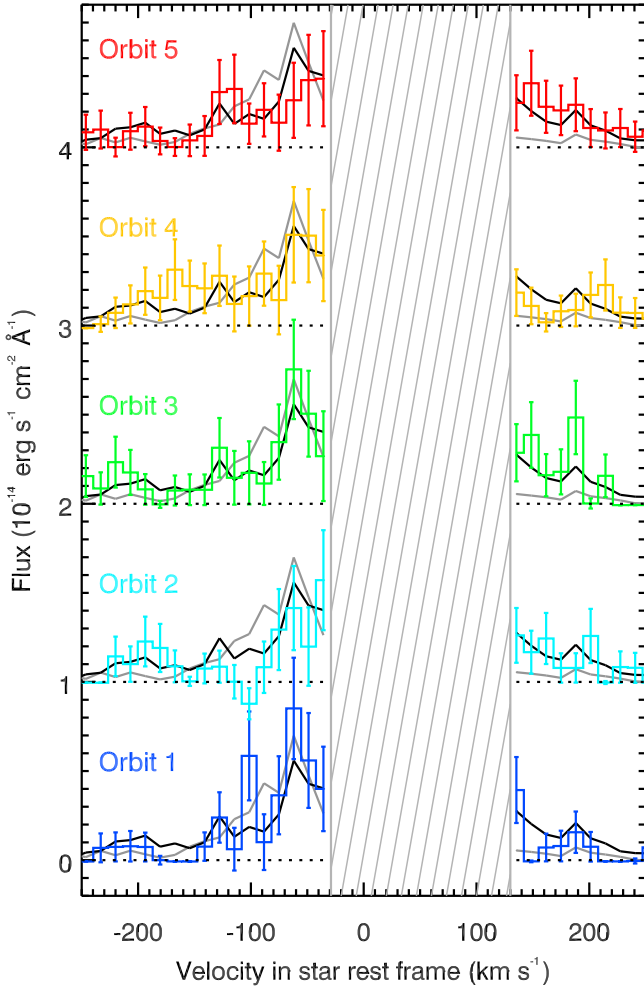


Figure 4. Ly α line spectra in Visit 4, overplotted with their average over the visit (black spectrum) and with the reference spectrum from B17 (gray spectrum). The spectra were shifted along the vertical axis (dotted black lines indicate the null level in each orbit). The dashed range is contaminated by air glow emission. The TRAPPIST-1 Ly α line is so faint that in some pixels no photons were detected over the duration of the exposure.

3. Analysis of TRAPPIST-1 FUV Observations

3.1. Long-term Evolution of the Stellar Ly α Line

A high-quality reference spectrum for the intrinsic stellar Ly α line of TRAPPIST-1 was built by B17 as the average of all spectra obtained in Visits 1, 2, and 3, excluding the spectral ranges contaminated by air glow emission or showing hints of flux variations. We first compared the Ly α line spectra obtained in each exposure of Visit 4 with this reference spectrum, searching for absolute flux variations over ranges covering more than STIS spectral resolution (about two pixels). As can be seen in Figure 4, the flux in the red wing of Visit 4 spectra is systematically higher than or equal to the reference spectrum, with a significant ($>3\sigma$) increase in orbits 2, 3, and 5. Similarly, the reference spectrum shows very little emission in the blue wing at velocities lower than about -160 km s^{-1} , whereas the flux in Visit 4 spectra is systematically higher than or equal to the reference in this range, with a marginal ($>2\sigma$) increase in orbits 2, 3, and 4. Therefore it comes as a surprise that Visit 4 displays an overall lower flux in the blue wing between about -120 and -55 km s^{-1} , with significant decreases in orbits 2 and 5 compared to the reference spectrum.

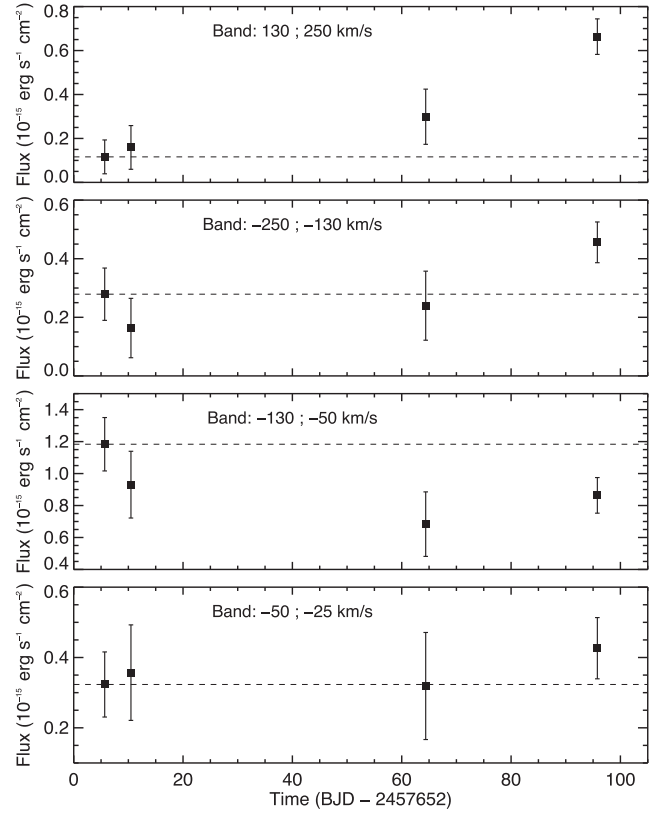


Figure 5. Evolution of the Ly α flux over time, integrated in four complementary bands (indicated in each panel). All spectra have been interpolated over a common wavelength table before being averaged in each visit. Each point thus corresponds to the mean spectrum over a visit. The dashed line indicates the flux level in Visit 1, measured outside of any planet transit.

To investigate the source of these differences, we studied the evolution of the Ly α line over the three-month span of our observations, averaging all spectra within each visit and integrating them in four complementary spectral bands (Figure 5). In agreement with the above spectral analysis, the flux in the symmetric wing bands ($\pm[130; 250] \text{ km s}^{-1}$) did not vary significantly from Visit 1 to Visit 3 (top panels in Figure 5) but increased noticeably in Visit 4. This variation likely traces an increase in the emission of the intrinsic stellar Ly α line (Section 3.2). However, while we do not expect similar absolute flux levels in the observed wing bands because of interstellar medium (ISM) absorption in the red wing of the Ly α line (see B17), it is surprising that the relative flux increase in Visit 4 is much larger and more significant in the red wing than in the blue wing. The flux in the blue wing even shows a marginal decline at lower velocities ($[-130; -50] \text{ km s}^{-1}$) from Visit 1 to Visit 4 (third panel in Figure 5), while the flux at velocities closer to the Ly α line core ($[-50; -25] \text{ km s}^{-1}$) remained at about the same flux level (bottom panel in Figure 5).

This comparison suggests that the shape of the line evolved between Visit 1 and Visit 4, with a change in the spectral balance of the Ly α line flux between the blue and the red wings. The search for absorption signatures possibly caused by the transit of TRAPPIST-1c in Visit 4 is made difficult by this evolution, since the spectra from Visits 1–3 cannot be used as a reference for the out-of-transit stellar line. We investigate this question in more detail in Section 3.3.

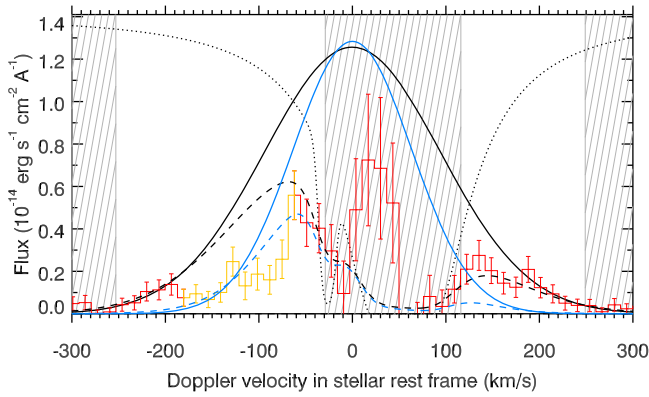


Figure 6. Ly α line profiles of TRAPPIST-1. Solid-line profiles correspond to our best estimates for the theoretical intrinsic Ly α line in Visits 1–3 (blue) and in Visit 4 (black). They yield the dashed-line profiles after ISM absorption and convolution by STIS LSF. The ISM absorption profile in the range 0–1 has been scaled to the vertical axis range and plotted as a dotted black line. The dashed-line profile in Visit 4 was fitted to the observations (red histogram, equal to the average of all spectra in Visit 4) outside of the hatched regions and excluding the variable range between -187 and -55 km s $^{-1}$ (highlighted in orange). Note that the model fits the observations well, even in the range contaminated by the air glow (except where it is strongest between 0 and 50 km s $^{-1}$).

3.2. High-energy Stellar Emission

To further study the evolution of the stellar Ly α line, we sought to reconstruct its intrinsic profile at the time of Visit 4 using the same approach as in B17. We assumed a Gaussian line profile, which was absorbed by the ISM using the column density derived in B17. The model was then convolved by the STIS line-spread function (LSF) and compared with the average of all spectra in Visit 4. We excluded the pixels beyond ± 250 km s $^{-1}$ from the fit, where the wings of the line become too faint. We also excluded the core of the line fully absorbed by the ISM and possibly biased by the air glow correction.

Contrary to the reconstruction performed in B17 on Visit 1–3 reference spectrum, in Visit 4, we found that it was not possible to fit the entire line profile well with our theoretical Gaussian model. Trying out different spectral ranges for the reconstruction, we found that a good fit was obtained when excluding the band $[-190; -55]$ km s $^{-1}$, even in the range contaminated by the air glow (Figure 6). This best-fit line profile for Visit 4 peaks at about the same flux level as the reference spectrum in Visits 1–3 but displays much broader wings, which is consistent with the stability of the Ly α line core and the variability of its wings noted in Section 3.1. Assuming this best-fit model is correct, it would suggest that both wings of the Ly α line have increased similarly from Visits 1–3 to Visit 4, but that the band $[-190; -55]$ km s $^{-1}$ is reabsorbed by an unknown source in this epoch. Alternatively, the intrinsic Ly α line of TRAPPIST-1 could have become asymmetric in Visit 4. Both scenarios would explain why the line profile observed in Visit 4 appears unbalanced between the blue and the red wing (see Section 3.1 and Figure 5). We further investigate this question in Section 3.3.

The Ly α line arises from different regions of the stellar atmosphere, ranging from the low-flux wings of the line formed in the colder regions of the lower chromosphere to the core of the line, which is emitted by the hot transition region between the upper chromosphere of the star and its corona. M dwarfs display a lower chromospheric emission than earlier-type stars but equivalent amounts of emission from the transition region

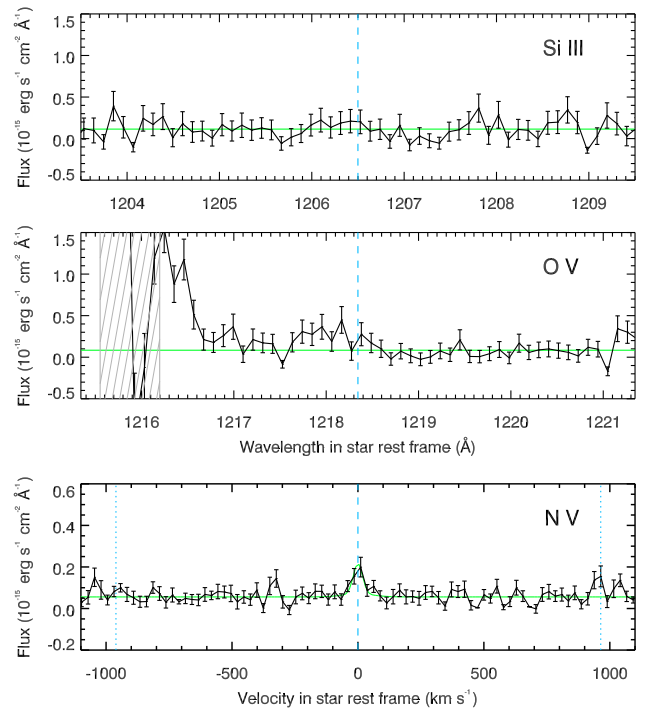


Figure 7. Average spectrum of TRAPPIST-1 in the star rest frame in the ranges of the Si III line (top panel), the O V line (middle panel), and the N V doublet (bottom panel). Pixels are binned by two for the sake of clarity. The blue dashed lines indicate the rest wavelength of the stellar lines. The green line is the mean flux in the range (excluding the region blueward of the O V line, since it is dominated by the red wing of the Ly α line). In the bottom panel, the lines of the N V doublet have been averaged in velocity space and fitted with a Gaussian model. Each N V line is indicated by a dotted blue line at the velocity of its transition relative to the other line of the doublet.

and the corona (see Youngblood et al. 2016 and references). This trend might be even more pronounced for late-type M dwarfs like TRAPPIST-1, since B17 suggested that this ultracool dwarf might have a weak chromosphere compared to its transition region and corona, based on its Ly α and X-ray emission (Wheatley et al. 2017) and the shape of its Ly α line. Interestingly, though, the broader wings of the TRAPPIST-1 Ly α line in Visit 4 might trace an increase in the temperature and emission of the stellar chromosphere.

In addition to the Ly α line, the spectral range of the STIS/G140M grating covers the Si III (1206.5 Å) and O V (1218.3 Å) transitions and the N V doublet (1242.8 and 1238.8 Å). We averaged our nine STIS spectra of TRAPPIST-1 to search for these stellar emission lines, and we detected the N V doublet (Figure 7). The two lines of the doublet were averaged and fitted with a Gaussian profile. Assuming that the width of the line is controlled by thermal broadening, we obtained a best-fit temperature on the order of 3×10^5 K, which is close to the peak emissivity of the N V lines at 2×10^5 K. We further derived a total flux in the doublet of about 7.3×10^{-17} erg s $^{-1}$ cm $^{-2}$. This line strength is consistent with the fits to the X-ray spectrum of TRAPPIST-1 by Wheatley et al. (2017), which predict N V line strengths of 1×10^{-17} and 100×10^{-17} erg s $^{-1}$ cm $^{-2}$ for two different models designed to span the possible range of EUV luminosities (the APEC and *cemekl* models, respectively). The dispersion is larger in the regions of the other stellar lines, and there is no clear evidence for their detection. More observations

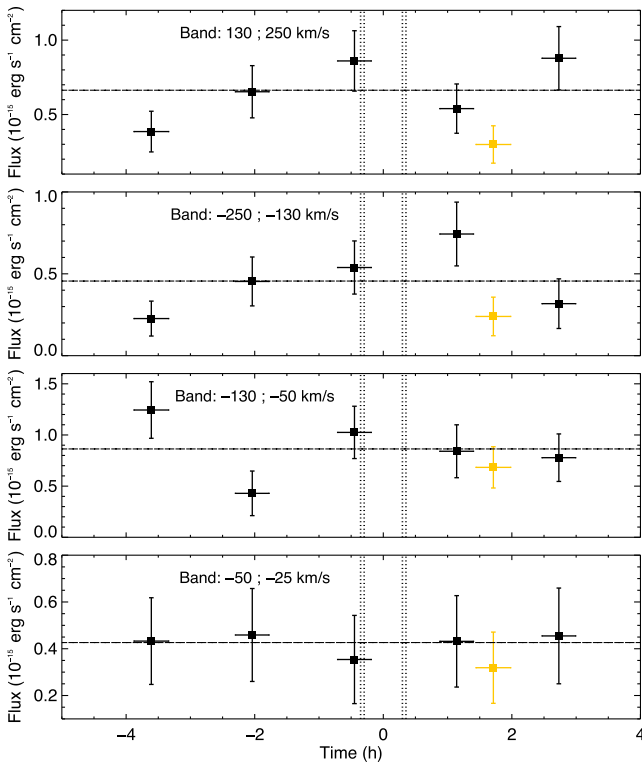


Figure 8. $\text{Ly}\alpha$ flux integrated in the same complementary bands as in Figure 5 and plotted as a function of time relative to the transit of TRAPPIST-1c. Vertical dotted lines indicate the transit contact times. Black points correspond to Visit 4, and the orange point to Visit 3. The dashed line is the mean flux in Visit 4.

will be required to characterize the chromospheric and coronal emission from TRAPPIST-1.

3.3. The Mysterious Shape of the TRAPPIST-1 $\text{Ly}\alpha$ Line

B17 reported a hint of absorption in the blue wing of the $\text{Ly}\alpha$ line in Visit 3, possibly caused by a hydrogen exosphere trailing TRAPPIST-1c. The long-term evolution of the intrinsic $\text{Ly}\alpha$ line prevents us from comparing the different visits to one another, and we thus took the average of all spectra in Visit 4 as a reference to search for the presence of an exosphere in this epoch. We highlight the long-term variability in Figure 8, where we plotted the flux integrated in the same spectral bands as in Figure 5 but phase-folded over the TRAPPIST-1c orbital period. The spectrum measured in Visit 3 shows a lower flux level at high velocities in the wing bands compared to the average flux in Visit 4 but similar flux levels in other parts of the line, consistent with the changes in the intrinsic line shape discussed in Section 3.1. No significant deviations to the average spectrum were found in Visit 4, and in particular no variations that would be consistent with the transit of an extended exosphere surrounding TRAPPIST-1c. More observations will be required to assess the possible short-term variability in the $\text{Ly}\alpha$ line and to search for residual absorption signatures.

If the $\text{Ly}\alpha$ line model derived in Section 3.2 corresponds to the actual intrinsic line of the star in Visit 4, what is the origin of the much lower flux observed in the band $[-190; -70] \text{ km s}^{-1}$ (Figure 6)? Despite our careful extraction of the stellar spectrum (Section 2), it is possible that the stronger air glow in this epoch was overcorrected at some wavelengths.

However, the air glow becomes negligible beyond about -100 km s^{-1} and therefore cannot explain the lower flux observed at larger velocities. If confirmed, this feature might imply that colder hydrogen gas is moving away from the star at high velocities and is absorbing about half of the $\text{Ly}\alpha$ flux in this velocity range. This absorption is unlikely to originate from TRAPPIST-1c alone, as it occurs in all orbits of Visit 4 and displays no correlation with the planet transit. Radiative braking is less efficient around TRAPPIST-1 than around the M2.5 dwarf GJ 436 (Bourrier et al. 2015) because its radiation pressure is about three times lower and thus more than five times lower than stellar gravity (B17). This could lead to the formation of giant hydrogen exospheres around the TRAPPIST-1 planets even larger than the one surrounding the warm Neptune GJ 436b (Ehrenreich et al. 2015) and possibly extending both behind and ahead of the planets because of gravitational shear (Bourrier et al. 2015). Furthermore, the XUV spectrum of TRAPPIST-1 (Section 4.2) yields photoionization lifetimes for neutral hydrogen atoms ranging from $\sim 20 \text{ hr}$ at the orbit of TRAPPIST-1b to nearly 600 hr at the orbit of TRAPPIST-1h (i.e., longer than the planetary period). Because of the very low $\text{Ly}\alpha$ and UV emission from TRAPPIST-1, neutral hydrogen exospheres could thus extend along the entire planetary orbits and could even cross the orbit of several planets. This suggests not only that some planets could be accreting the gas escaped from their companions, but also that a large volume of the TRAPPIST-1 system could be filled with neutral hydrogen gas, providing a possible explanation for the persistent absorption signature in Visit 4. Given that the evaporating planets sustaining this system-wide hydrogen cloud would be in different relative positions at a given epoch, the structure of the cloud and its absorption signature would be highly variable over time, which could explain why it was not detected in Visit 1. We note, though, that the hydrogen cloud would still have to be accelerated to very high velocities away from the star (possibly through charge exchange with the stellar wind; Holmström et al. 2008; Ekenbäck et al. 2010; Bourrier et al. 2016b) to explain the velocity range of the measured absorption.

Alternatively, this variation could have a stellar origin. This is also an intriguing possibility, because the $\text{Ly}\alpha$ line of TRAPPIST-1 was well approximated with a Gaussian profile in previous visits (B17) and the $\text{Ly}\alpha$ line profiles of later-type M dwarfs do not show evidence for strong asymmetries (e.g., Bourrier et al. 2015; Youngblood et al. 2016). The intrinsic $\text{Ly}\alpha$ line of TRAPPIST-1 might have become asymmetric in Visit 4 because of variations in the up-flows and down-flows of stellar hydrogen gas, or because of absorption by colder hydrogen gas at high altitudes in the stellar atmosphere. Filaments made of partially ionized plasma are, for the Sun, a hundred times cooler and denser than the coronal material in which they are immersed, and can thus be optically thick in the $\text{Ly}\alpha$ line (e.g., Parenti 2014). The large velocities of the putative absorber of the TRAPPIST-1 $\text{Ly}\alpha$ line might indicate that we witnessed the eruption of a filament that was expelled by a destabilization of the stellar magnetic field. Such eruptions can reach large distances and velocities (between 100 and 1000 km s^{-1} for the Sun, e.g., Schrijver et al. 2008). In any case, our new observations of TRAPPIST-1 raise many questions about the physical mechanisms behind the emission of the $\text{Ly}\alpha$ line in an ultracool dwarf.

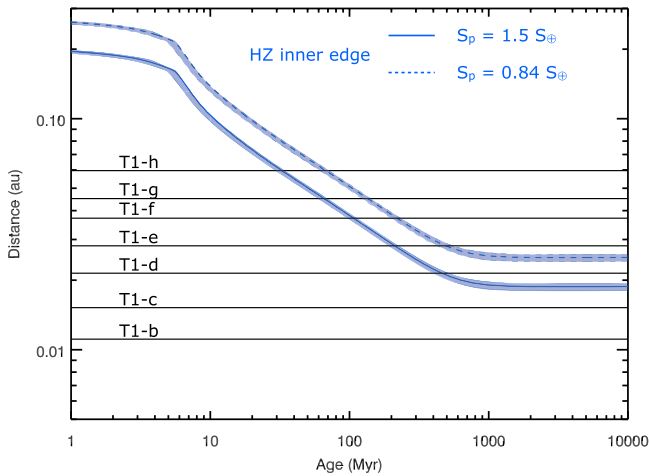


Figure 9. Architecture of the TRAPPIST-1 system and evolution of the inner edge of the HZ for two different hypotheses: a synchronized planet ($S_p = 1.5 S_\oplus$, see Yang et al. 2013) and a nonsynchronized planet ($S_p = 0.84 S_\oplus$, see Kopparapu 2013). The thick blue line corresponds to HZ inner edges, which were calculated from evolutionary models for a $0.091 M_\odot$ dwarf (Section 4). The blue areas correspond to the uncertainties on the HZ inner edge due to the uncertainty of the mass of the star.

Despite these unknowns, our best-fit Gaussian profile can be used to estimate a conservative upper limit on the total Ly α irradiation of the planets at the epoch of Visit 4 (Section 4.2). More observations of TRAPPIST-1 at Ly α will be required to beat down the photon noise, to assess the effects of stellar variability, and to reveal absorption signatures caused by the putative planets’ exospheres. The long-term variability of the TRAPPIST-1 Ly α line emphasizes the need for contemporaneous observations obtained outside and during the planet’s transits.

4. Evolution of the Planets under High-energy Irradiation

Two types of spectral radiation are involved in the escape of water from an exoplanet: far UV (FUV, 100–200 nm) to photodissociate water molecules and XUV (0.1–100 nm) to heat up the upper atmosphere and allow for the escape of the photodissociation products, hydrogen and oxygen (e.g., Lammer et al. 2003; Vidal-Madjar et al. 2003). In this section, we study the evolution of water loss from the TRAPPIST-1 planets, in particular during their runaway greenhouse phase (see Barnes & Heller 2013; Luger & Barnes 2015; and Bolmont et al. 2017 for generic brown dwarfs and M dwarfs and Ribas et al. 2016 and Barnes et al. 2016 for the M dwarf planet Proxima-b). The idea is that, once a planet reaches the HZ, its water can recombine and condense. Thus the amount of water reaching the upper layers of the atmosphere would be much lower than the amount available during a runaway phase. With a low mass of $0.0802 \pm 0.0073 M_\odot$, TRAPPIST-1 (stellar type M8) is just above the limit between brown dwarfs and M dwarfs and is expected to cool down for about 1 Gyr before reaching the main sequence. During this initial phase, all TRAPPIST-1 planets, including those in the HZ today (planets e, f, and g according to Gillon et al. 2017), were hot enough for the water potentially delivered during the formation process to be injected in gaseous form into the atmosphere and lost more easily (Jura 2004; Selsis et al. 2007).

In a first step, we estimated the duration of the runaway greenhouse phases for the TRAPPIST-1 planets. Figure 9 shows

the present-day orbital distances of the seven planets and the evolution of the HZ inner limits for a TRAPPIST-1 analog. Using the mass of TRAPPIST-1 ($0.0802 M_\odot$) yielded an HZ inner edge much closer to what is shown in Gillon et al. (2017), because low-mass star evolution models tend to underestimate the luminosity for active stars (Chabrier et al. 2007) such as TRAPPIST-1 (Luger et al. 2017; Vida et al. 2017). We therefore revised the stellar mass for TRAPPIST-1 following the prescription of Chabrier et al. (2007), by greatly reducing convection efficiency in CLES (Code Liégeois d’Évolution Stellaire) stellar evolution models (Scuflaire et al. 2008). We estimate a stellar mass of $0.091 \pm 0.005 M_\odot$ using TRAPPIST-1’s luminosity (Filippazzo et al. 2015), density, and metallicity (Gillon et al. 2017) as inputs. The error bars include uncertainties associated with these input parameters, as well as on the initial helium abundance. This stellar mass is fully consistent with the most recent dynamical mass estimates based on ultracool binaries for TRAPPIST-1’s spectral type (Dupuy & Liu 2017) and with the larger radius derived by Burgasser & Mamajek (2017). The inferred age is greater than 2 Gyr (the star evolves too slowly to constrain its age through stellar evolution models), consistent with the 3–8 Gyr (Luger et al. 2017) and 7.6 ± 2.2 Gyr (Burgasser & Mamajek 2017) age estimates for TRAPPIST-1. The evolution of the HZ inner edge was calculated for two different assumptions regarding the rotation of the planets. The first one ($S_p = 1.5 S_\oplus$, where S_p is the insolation received by the planet and S_\oplus the solar insolation received by the Earth) corresponds to a synchronized planet. This estimation comes from Yang et al. (2013), which showed that a tidally locked planet could sustain surface liquid water closer to the star due to the protection of the substellar point by water clouds. The second one ($S_p = 0.84 S_\oplus$) is the classical limit, computed for a nonsynchronous planet (Kopparapu 2013). Note that the planet does not require as much incident flux as the Earth to maintain the same surface temperature because of the redness of the star. For instance, the albedo of ice and snow is significantly lower in the infrared (Joshi & Haberle 2012), which means that the temperature of a planet is higher around TRAPPIST-1 than around a solar-type star for a given flux, and therefore the inner edge of the HZ corresponds to a lower incoming flux. We estimated the age at which the planets entered the shrinking HZ (Table 3), considering that their migration stopped when the gas disk dissipated (Luger et al. 2017; Tamayo et al. 2017). This age corresponds to the end of the runaway greenhouse phase, and we found it lasted between a few 10 Myr (for planet h) to a few 100 Myr (for planet d in the synchronized scenario). The HZ stabilized at about 1 Gyr, earlier than the lower limit on the age of TRAPPIST-1 given by Luger et al. (2017). This suggests that planets d to h have already been subjected to the strongest phases of their atmospheric erosion, but that planets b and c might still be in their runaway greenhouse phase if they were formed with enough water.

4.1. Water Loss Model

We calculated mass loss rates from TRAPPIST-1 planets using an improved formalism based on the energy-limited formula (e.g., Lecavelier des Etangs 2007; Selsis et al. 2007; Luger & Barnes 2015):

$$\dot{M}^{\text{tot}} = \epsilon \left(\frac{R_{\text{XUV}}}{R_p} \right)^2 \frac{3 F_{\text{XUV}}(a_p)}{4 G \rho_p K_{\text{tide}}}, \quad (1)$$

Table 3
Age at Which the TRAPPIST-1 Planets Enter the HZ for Two Different Hypotheses: A Synchronized Planet ($S_p = 1.5 S_\oplus$)
and a Nonsynchronized Planet ($S_p = 0.84 S_\oplus$)

Assumption On HZ Limit	T_{HZ} (Myr)						
	Planet b	Planet c	Planet d	Planet e	Planet f	Planet g	Planet h
$S_p = 1.5 S_\oplus$	461	211	107	65	33
$S_p = 0.84 S_\oplus$	494	218	135	67

Table 4
High-energy Emission from TRAPPIST-1

Wavelength Domain	XUV (0.5–100 nm)		Ly α	
	L_{XUV} (erg s $^{-1}$)	$\log_{10}(L_{\text{XUV}}/L_{\text{bol}})$	Ly α (erg s $^{-1}$)	$\log_{10}(\text{Ly}\alpha/L_{\text{bol}})$
Lower estimate	5.26×10^{26}	−3.58	1.44×10^{26}	−4.15
Mean estimate	6.28×10^{26}	−3.51	1.62×10^{26}	−4.09
Upper estimate	7.30×10^{26}	−3.44	1.81×10^{26}	−4.05

with $F_{\text{XUV}}(a_p)$ the XUV irradiation. The heating efficiency ϵ is the fraction of the incoming energy that is transferred into gravitational energy through mass loss. As in Bolmont et al. (2017) and Ribas et al. (2016), we calculated ϵ using 1D radiation hydrodynamic mass loss simulations based on Owen & Alvarez (2016). The efficiency ϵ varies with the incoming XUV radiation. For example, for today’s estimated XUV flux (see next section and Table 4), we obtain values of 0.064, 0.076, 0.089, 0.099, 0.107, 0.112, and 0.115, respectively, for planets b to h. These efficiencies are on the same order as the 10% assumed by Wheatley et al. (2017) but larger than the 1% assumed by Bourrier et al. (2017).

In the following sections, we consider a constant XUV flux and an evolving XUV flux. For the latter assumption, ϵ is computed accordingly. In the energy-limited formula, the parameter $\left(\frac{R_{\text{XUV}}}{R_p}\right)^2$ accounts for the increased cross-sectional area of planets to XUV radiation, while K_{tide} accounts for the contribution of tidal forces to the potential energy (Erkaev et al. 2007). Both are set to unity for these cool and small planets (Bolmont et al. 2017). The mean density of the planets was calculated using masses derived from TTV in Gillon et al. (2017; see Table 1). We consider here that the atmospheres of the planets are mainly composed of hydrogen and oxygen and compute their joint escape using the formalism of Hunten et al. (1987). The escape rates of both elements depend on the temperature of the thermosphere, the gravity of the planet, and a collision parameter between oxygen and hydrogen. As in Bolmont et al. (2017) and Ribas et al. (2016), we adopt a thermosphere temperature of 3000 K, obtained through our hydrodynamic simulations. We caution that more detailed models, including FUV radiative transfer, photochemical schemes, and non-LTE kinetics in the rarefied gas regions of the upper atmosphere, will be required to determine accurately the outflow properties. For example, the hydrodynamic outflow of hydrogen could drag water molecules, which are only slightly heavier than oxygen atoms, upward, and they would be photodissociated at high altitudes into more escaping oxygen and hydrogen atoms. Nonetheless, our assumptions likely maximize the XUV-driven escape (see Bolmont et al. 2017), and our estimates of the water loss should be considered as upper limits.

4.2. Estimation of the XUV Irradiation of the Planets

To calculate the planetary mass losses, we needed estimations of the XUV irradiation from TRAPPIST-1 over the whole history of the system. In a first step, we calculated the present-day stellar irradiation. We used the same value as in Bourrier et al. (2017) for the X-ray emission (5–100 Å), studied by Wheatley et al. (2017). The stellar EUV emission between 100 and 912 Å is mostly absorbed by the ISM but can be approximated from semiempirical relations based on the Ly α emission. The theoretical Ly α line profile derived for Visit 4 (Section 3.2) yields an upper limit on the total Ly α emission of $7.5 \pm 0.9 \times 10^{-2} \text{ erg s}^{-1} \text{ cm}^{-2}$ at 1 au. This is larger than the emission derived for previous visits ($5.1^{+1.9}_{-1.3} \times 10^{-2} \text{ erg s}^{-1} \text{ cm}^{-2}$, B17), in agreement with the increase in flux suggested by observations (Section 3.1). We chose to consider those two estimates as lower and upper limits on the present Ly α emission of TRAPPIST-1, and we used the Linsky et al. (2014) relation for M dwarfs to derive corresponding limits on the EUV flux. Table 4 gives our best estimate for today’s range of fluxes emitted by TRAPPIST-1 at Ly α and between 5 and 912 Å. We computed the ratio of these two fluxes to the bolometric luminosity and obtained a value of $\log_{10}(L_{\text{XUV}}/L_{\text{bol}})$ between −3.39 and −3.73, which is about a factor of 2.5 lower than that estimated from the X-ray flux by Wheatley et al. (2017).

In a second step, we estimated the past stellar irradiation. We consider that when the planets were embedded in the protoplanetary disk, they were protected from irradiation and did not experience mass loss. In that frame, water loss began at the time when the disk dissipated, which we assume to be 10 Myr (Pascucci et al. 2009; Pfalzner et al. 2014; Pecaute & Mamajek 2016). We investigated two different scenarios, depending on our assumptions for the temporal evolution of the XUV emission after the disk dissipation:

1. A constant L_{XUV} equal to today’s range of emission. This assumption might be supported by the X-ray flux of TRAPPIST-1, which is consistent with a saturated emission typical of earlier-type M dwarfs, according to Wheatley et al. (2017).
2. An evolving L_{XUV} , considering the ratio $L_{\text{XUV}}/L_{\text{bol}}$ to be constant throughout the history of the star. The ratio was set to the present-day estimate of the star luminosities (see Table 4). We used the evolutionary models of

Table 5
Current Mass Loss Rate, Hydrogen Loss Rate, and Oxygen Loss Rate for the TRAPPIST-1 Planets

Planet	b	c	d	e	f	g	h
Mass loss ($M_{\text{ocean}}/\text{Myr}$)	8.2×10^{-3}	2.9×10^{-3}	2.3×10^{-3}	1.7×10^{-3}	1.4×10^{-3}	6.4×10^{-4}	2.9×10^{-4}
Hydrogen loss (g s^{-1})	4.3×10^7	2.3×10^7	1.3×10^7	1.2×10^7	1.1×10^7	1.2×10^7	4.3×10^6
Oxygen loss (g s^{-1})	2.9×10^8	1.0×10^8	8.2×10^7	5.7×10^7	4.7×10^7	1.5×10^7	7.5×10^6

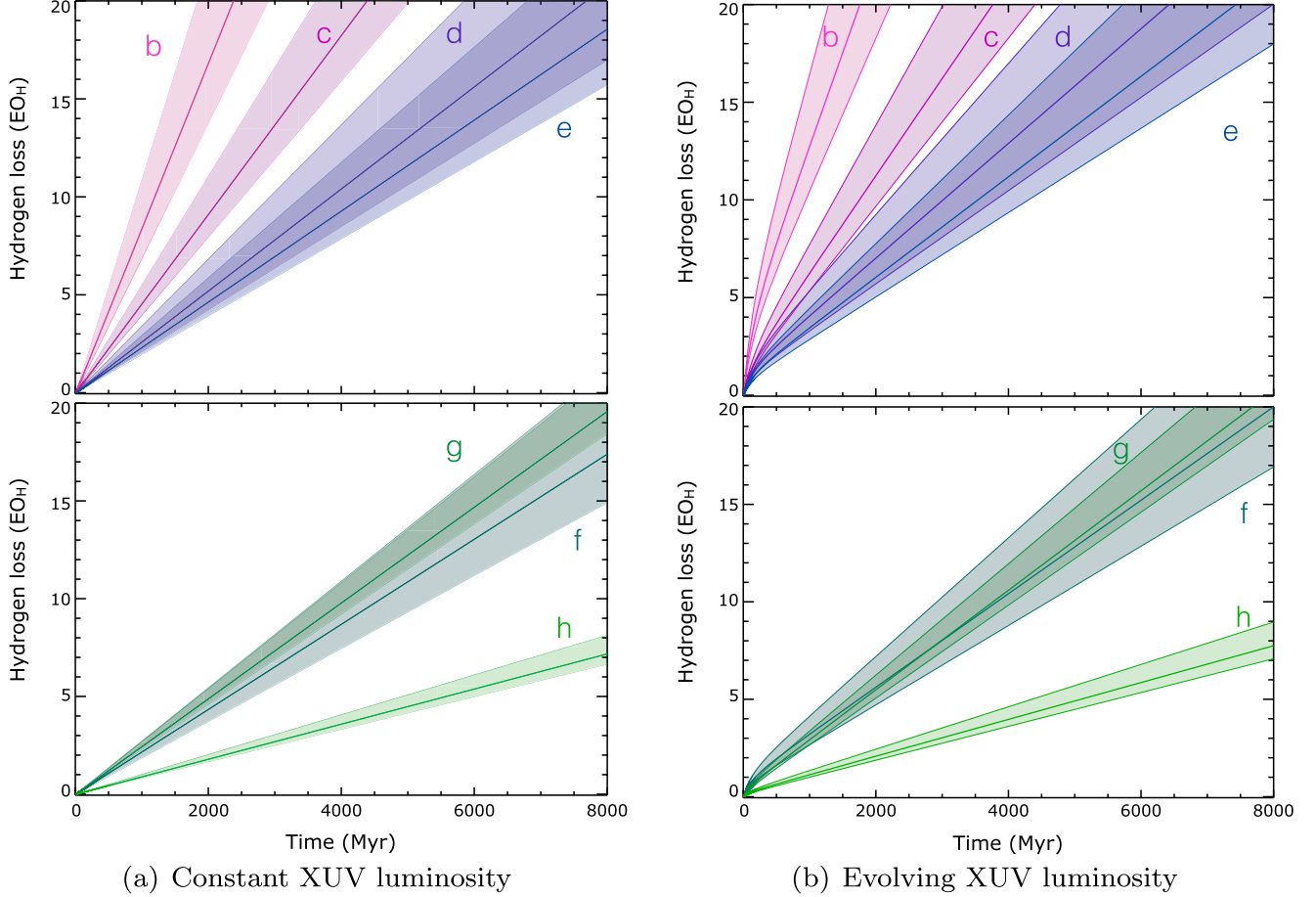


Figure 10. Cumulative hydrogen loss for the TRAPPIST-1 planets for the two different assumptions for the evolution and values of the XUV flux (see Table 4). The masses of the planets are the masses from Table 1. Because of our assumptions, these estimates likely represent upper limits on the actual loss.

Baraffe et al. (2015) to compute the evolution of the bolometric luminosity.

Here we set the stellar mass to its nominal value of $0.091 M_{\odot}$. Considering the range allowed by the uncertainties would slightly change our water loss estimates, at the time the planet reached the HZ for the constant XUV flux prescription and at all ages for the evolving XUV flux prescription. We estimate that the difference would be less than 4% at an age of 8 Gyr.

4.3. Water Loss Evolution

Using the energy-limited model in Section 4.1 and our estimates for the XUV irradiation in Section 4.2, we calculated the mass loss from TRAPPIST-1 planets over time. In order to calculate the hydrogen loss, we used method (2) of Ribas et al. (2016), which consists in calculating the ratio between the oxygen and hydrogen fluxes as a function of the XUV luminosity. We consider here an infinite water reservoir. This

allows us to consider that the ratio of hydrogen and oxygen remains stoichiometric even though the loss is not stoichiometric. This provides us with an upper limit on the mass loss (see Ribas et al. 2016 for a discussion on the effect of a finite initial water reservoir). The loss is given in units of Earth-ocean-equivalent content of hydrogen (referred to as $1 EO_H$). In other words, the mass loss is expressed in units of the mass of hydrogen contained in one Earth ocean (1.455×10^{20} kg, with an Earth ocean mass corresponding to 1.4×10^{21} kg). For example, we estimate a current mass loss from planet b of $0.008 M_{\text{ocean}}/\text{Myr}$ for the nominal XUV flux (Table 4). This corresponds to escape rates of oxygen and hydrogen from planet b of $2.9 \times 10^8 \text{ g s}^{-1}$ and $4.3 \times 10^7 \text{ g s}^{-1}$, respectively. The values for the other planets can be found in Table 5. Figure 10 shows the evolution of the hydrogen loss from the TRAPPIST-1 planets as a function of the age of the system in the two scenarios assumed for the evolution of the XUV flux. Table 6 gives the corresponding mass loss at different times of interest.

Table 6
Cumulative Hydrogen Loss (in EO_H) for Different Times (Table Corresponding to Figure 10)

	Planet	Mass (M_\oplus)	H loss (EO_H)			
			T_{HZ} ($1.5 S_\oplus$)	T_{HZ} ($0.84 S_\oplus$)	3 Gyr	8 Gyr
L_{XUV} evol	b	0.85	29.2–35.4	71.5–86.9
	c	1.38	15.2–17.6	38.1–44.1
	d	0.41	2.35–2.87	...	9.12–11.2	22.2–27.2
	e	0.62	1.20–1.46	2.05–2.49	7.98–9.57	19.6–23.4
	f	0.68	0.70–0.86	1.14–1.39	7.46–8.89	18.4–21.8
	g	1.34	0.31–0.37	0.58–0.67	7.79–8.46	20.1–21.7
	h	0.46	0.07–0.09	0.14–0.17	2.91–3.23	7.40–8.15
L_{XUV} cst	b	0.85	25.3–30.7	67.5–82.1
	c	1.38	13.7–15.8	36.5–42.1
	d	0.41	1.17–1.44	...	7.80–9.57	20.8–25.5
	e	0.62	0.47–0.56	1.12–1.34	6.95–8.28	18.6–22.1
	f	0.68	0.21–0.25	0.45–0.54	6.52–7.70	17.4–20.6
	g	1.34	0.14–0.15	0.31–0.33	7.34–7.89	19.6–21.1
	h	0.46	0.02–0.02	0.05–0.06	2.69–2.94	7.18–7.86

Note. The parameter T_{HZ} is the age at which a planet enters the HZ (see Table 3). The two values given for each column correspond to the uncertainty coming from the different luminosity prescriptions (between low and high; see Table 4).

Planets b and c never reach the HZ, so they are expected to have lost water via the runaway greenhouse mechanism (Section 4) throughout the full lifetime of the star. If TRAPPIST-1 is 3 Gyr old (the lower estimate of the age given in Luger et al. 2017), planet b potentially lost more than 20 EO_H and planet c more than 10 EO_H . If planets b and c formed with an Earth-like water content, they are likely dry today, whatever the assumptions on the XUV flux and the age of the star. Alternatively, they might have formed as ocean planets (Léger et al. 2004), in which case a loss of 20 Earth oceans for planet b would represent only 0.5% of its mass. Currently this scenario is not favored by the planet formation model proposed by Ormel et al. (2017), which excludes water fractions larger than about 50%, and by the densities of planets b and c derived observationally by Gillon et al. (2017) and Wang et al. (2017), although we note that they still allow for a significant water content.

If we consider that the water loss only occurs during the runaway phase, planets d to f lost less than 4 EO_H before reaching the HZ, and planets g and h lost less than 1 EO_H . In that scenario, the outer planets of the TRAPPIST-1 system might thus still harbor substantial amounts of water, especially planets e to h if the low densities derived by Wang et al. (2017) are confirmed. What if hydrodynamic water loss continued once the planets reached the HZ? After 3 Gyr, we estimate that planet g and those closer in would have lost more than 7 EO_H . After 8 Gyr, they would have lost more than 20 EO_H (Table 6). Interestingly, the relation obtained by Guinan et al. (2016) for M0–5 V dwarf stars yields an age of about 7.6 Gyr for TRAPPIST-1, using the X-ray flux obtained by Wheatley et al. (2017) in the *ROSAT* band ($0.14 \text{ erg s}^{-1} \text{ cm}^{-2}$ at 1 au). This age is at the upper limit of the range derived by Luger et al. (2017), and if confirmed it suggests that all TRAPPIST-1 planets have lost substantial amounts of water over the long history of the system. Refined estimates of the planet densities will, however, be necessary to determine whether they still harbor a significant water content. We also note that our estimates for the water loss once planets are in the HZ (Table 6) are probably upper limits. If the planet is able to retain its background atmosphere, the

tropopause is expected to act as an efficient cold trap, preventing water from reaching the higher parts of the atmosphere (e.g., Wordsworth & Pierrehumbert 2014; Turbet et al. 2016). In that case, water escape would be limited by the diffusion of water through the cold trap. However, if the background pressure is low, the water vapor mixing ratio increases globally in the atmosphere (Turbet et al. 2016), and hydrogen escape is no longer limited by the diffusion of water. The farther out the TRAPPIST-1 planets, the more likely they would have been able to sustain an important background atmosphere, thus protecting the water reservoir once in the HZ.

4.4. Consequences of the Uncertainty on the Planetary Masses

While the radii of the TRAPPIST-1 planets are known to a good precision, their masses remain very uncertain. We set today's XUV luminosity to the nominal estimate in Table 4, and we investigated the effect of changing the value of the planetary mass within the range of uncertainty estimated by Gillon et al. (2017; see Table 1). For planet h, we investigated a range of compositions from 100% ice to 100% iron, which corresponds to masses between $0.06 M_\oplus$ and $0.86 M_\oplus$. Figure 11(b) shows that for most planets the uncertainty on their mass dominates the final uncertainty on the mass loss, compared to the effect of varying the XUV irradiation with its uncertainty (see also Luger & Barnes 2015). This is because hydrogen loss is not only inversely proportional to the planetary mass (see Equation (1)) but also linked to the ratio of the escape fluxes of hydrogen and oxygen ($r_F = F_O/F_H$), which is a function of the crossover mass (see Hunten et al. 1987; Bolmont et al. 2017). For a given value of the XUV luminosity and an infinite initial water reservoir, the hydrogen mass loss is described by a polynomial in M_p of the form $\alpha/M_p + \beta M_p$, where α and β are constants depending, for example, on the radius of the planet (we refer to Equations (8) and (9) of Bolmont et al. 2017 to derive these values). The mass flux decreases with increasing planetary mass, and the ratio of the flux of oxygen over the flux of hydrogen decreases with increasing planetary mass. For high masses, the mass flux is lower (gravity wins over cross section), but the mass loss mainly

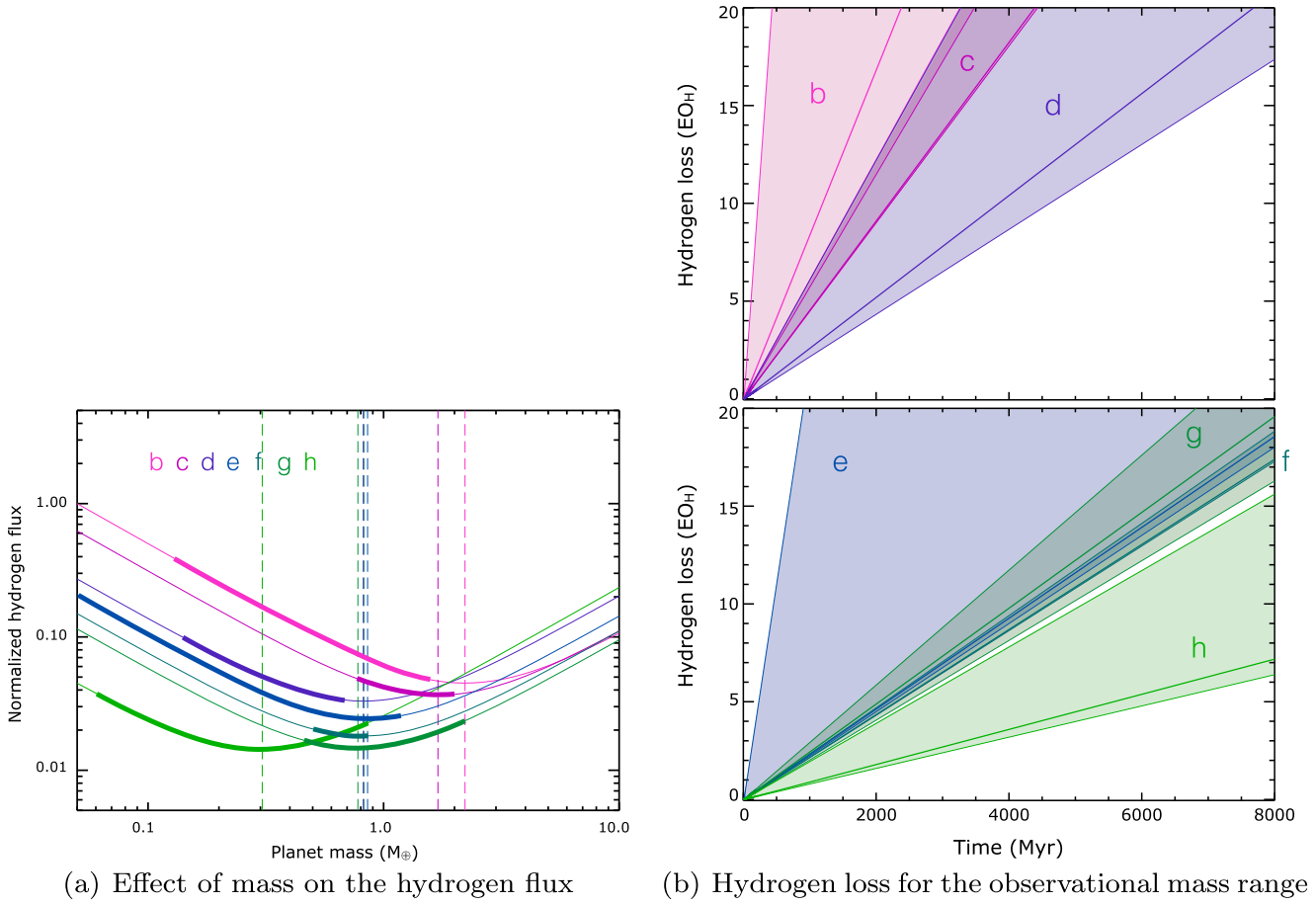


Figure 11. Effect of planetary mass on the hydrogen loss for the TRAPPIST-1 planets, for the range of masses in Gillon et al. (2017). The XUV flux is set to its nominal estimate ($L_{XUV} = \text{cst}$). (a) Normalized hydrogen flux as a function of planetary mass for the different planets. The thick part of each curve corresponds to the allowed range determined by Gillon et al. (2017), and the vertical line corresponds to the mass that corresponds to the lowest hydrogen flux. (b) Hydrogen loss from the planets. The thicker line corresponds to the loss calculated for the mass given in Gillon et al. (2017), and the thin lines correspond to the lower and upper estimations within the mass range given in the same article.

occurs via hydrogen escape. This results in a high hydrogen escape rate. For low masses, the outflow is a mixture of hydrogen and oxygen, meaning less hydrogen escapes for an equal energy input, but the overall mass flux is higher. For a low-enough mass, the increased overall mass flux does more than compensate, and this also results in a high hydrogen loss. The hydrogen loss is therefore high for very low mass and very high mass planets with a minimum for intermediate mass. Figure 11(a) shows this dependence of the hydrogen flux with mass for each planet of the system. For all planets but planet b, the minimum loss is achieved for an intermediate mass in the range allowed by the observations (this range is displayed as a thicker line on the graph). The lower curves delimiting the colored areas in Figure 11(b) correspond to the hydrogen loss calculated for this intermediate mass for all planets but b. For planet b, the minimum hydrogen loss is obtained for the highest mass allowed by the observations.

In the end, the uncertainty on the hydrogen loss comes mainly from the uncertainty on mass rather than the uncertainty on the prescribed luminosity (although we note that our calculations assume an unlimited water supply, yielding upper limits on the water losses; see Section 4.3). The uncertainty on the hydrogen loss thus ranges from about 80% for planets b and e to $\sim 50\%$ for planets d and h, $\sim 20\%$ for planet c and g, and only 4% for planet f. Table 7 gives the upper and lower

estimates of hydrogen loss for the mass range for each planet and for the different times considered in this study. Due to the relative precision of the mass of planet f, the mass loss is relatively well constrained with our model, with a loss of less than $0.5 EO_H$ before reaching the HZ and less than $20 EO_H$ at an age of 8 Gyr. Given that the low density of planet f is compatible with a nonnegligible water content (Gillon et al. 2017), this could indicate that water loss may not have been a very efficient process or that the planet formed with a large fraction of its mass in water.

We note that for most planets, the estimates of the masses from Wang et al. (2017) are more precise but are consistent compared to Gillon et al. (2017). However, for planet f, the mass ranges obtained by these different studies are incompatible, and using the mass from Wang et al. (2017) would lead to a higher mass loss than what is shown on Figure 11(b). More data are needed to refine our measurements of the masses of the planets of the system.

5. Hydrogen Loss versus Hydrogen Production

5.1. Photolysis

The atmospheric mass loss can be limited by the amount of hydrogen formed by photodissociation of water molecules. We computed the rate of hydrogen production driven by the FUV

Table 7
Cumulative Hydrogen Loss (in EO_H) for Different Times

		H loss (EO_H)				Uncertainty	
	Planet	Mass range (M_\oplus)	T_{HZ} ($1.5 S_\oplus$)	T_{HZ} ($0.84 S_\oplus$)	3 Gyr	8 Gyr	Range %
L_{XUV} cst	b	0.13–1.57	18.8–160	50.3–429	79
	c	0.77–1.99	14.5–19.2	38.6–51.3	14
	d	0.14–0.68	1.04–3.16	...	6.97–21.0	18.6–56.0	50
	e	0.04–1.20	0.49–5.21	1.17–12.5	7.26–77.6	19.4–207	83
	f	0.50–0.86	0.23–0.25	0.48–0.55	6.99–7.88	18.7–21.0	6
	g	0.46–2.22	0.12–0.19	0.28–0.43	6.60–10.3	17.6–27.5	22
	h	0.06–0.86	0.02–0.05	0.05–0.13	2.59–6.84	6.92–18.3	45

Note. The parameter T_{HZ} is the age at which a planet enters the HZ (see Table 3). The two values given for each column correspond to the uncertainty coming from the masses (for the mean estimation of the XUV luminosity, see Table 4).

part of the spectrum, which is taken to be restricted to the Ly α emission (as in Bolmont et al. 2017). We note that water molecules could further be dissociated through impact with high-energy electrons, in particular those produced by the ionization of water (considering the high X-ray emission of TRAPPIST-1 and the large ionization cross section of water in the XUV; Heays et al. 2017). Figure 12 shows the hydrogen loss for the nominal irradiation (Table 4) and planet masses, and the hydrogen quantity available due to photodissociation of water for two different efficiencies: $\epsilon_\alpha = 1$ (each photon leads to a dissociation; see Bolmont et al. 2017) and 0.2. We obtained the following results for a constant XUV luminosity:

1. For planets b and c, photodissociation is not the limiting process for high efficiencies. The hydrogen loss is limited by the hydrodynamic escape as computed in the previous section;
2. For planets d to g, photodissociation is the limiting process whatever the efficiency: the rate of hydrogen formation by photodissociation is below the escape rate of hydrogen.

Photodissociation of water also becomes the limiting process for planets b and c if $\epsilon_\alpha \simeq 0.60$. Because of various processes, such as photon backscattering or recombination of hydrogen atoms, only a fraction of the incoming FUV photons actually result in the loss of a hydrogen atom. As a result, we do not expect photodissociation to be more efficient than 20% (Bolmont et al. 2017). It should be the limiting process for all planets, and the mass losses estimated in Section 4 can be considered as upper limits. The quantity of hydrogen available from photolysis assuming a 20% efficiency is given in Table 8 for each planet, to be compared with the hydrodynamic hydrogen loss. We note that the photolysis process does not depend on the mass of the planets (only on their radii, known to a high precision for the TRAPPIST-1 planets), so these results are more robust than the hydrogen loss estimates, which highly depend on the mass of the planets.

5.2. Outgassing

Water is contained within a rocky planet’s mantle in the form of hydrated minerals, as unbound fluids, or in melt. This water can be released to the surface through volcanic activity. Such outgassing processes are very different during the early stages of planet evolution (<10–100 Myr; see Solomatov 2007), where the surface and a significant fraction of the planet’s

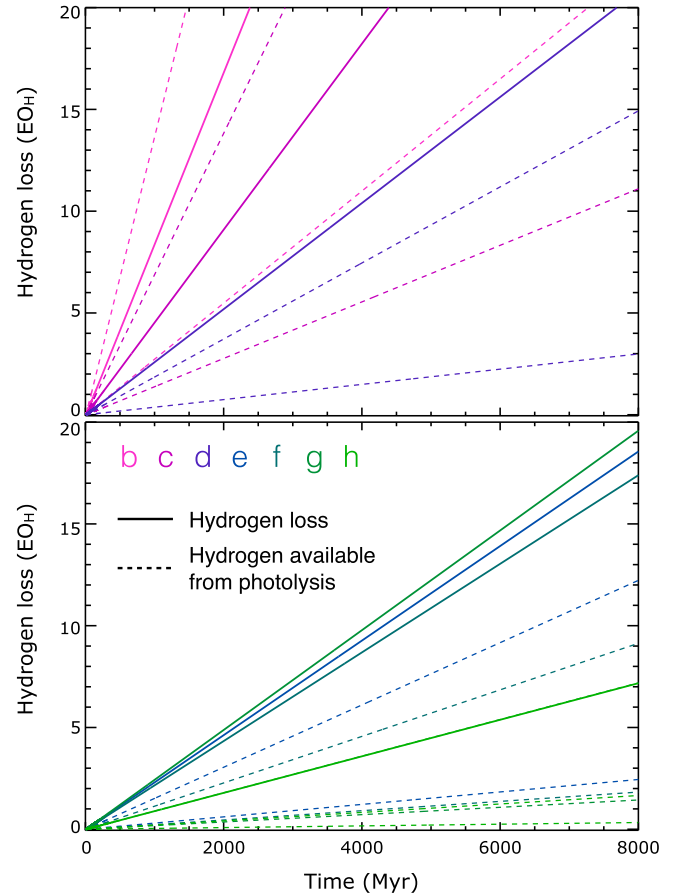


Figure 12. Hydrogen loss (solid lines) and hydrogen production (dashed lines) by photolysis for the planets of TRAPPIST-1. The amount of hydrogen formed by photolysis was calculated for two efficiencies of the process: 1 (upper dashed lines) and 0.2 (lower dashed lines). With a realistic value of the photolysis efficiency, we find that photolysis is the limiting process as the hydrogen loss cannot occur faster than the hydrogen production.

mantle could be molten (magma ocean phase), and at a later stage, where the largest fraction of the planet’s mantle is solid. In the following sections, we will discuss the amounts of outgassed water during the magma ocean phase of the TRAPPIST-1 planets, assuming they are rocky, and we compute the water outgassing rates for the later stage of subsolidus convection as a function of time.

Table 8
Hydrogen Loss and Hydrogen Production (in EO_H) for Different Times

	Planet	Mass (M_\oplus)	H loss (EO_H)			
			T_{HZ} ($1.5 S_\oplus$)	T_{HZ} ($0.84 S_\oplus$)	3 Gyr	8 Gyr
L_{XUV} evol	b	0.85	32.4– 13.0	79.5– 28.6
	c	1.38	16.5– 6.54	41.2– 14.4
	d	0.41	2.62– 0.65	...	10.2– 1.76	24.8– 3.88
	e	0.62	1.33– 0.39	2.28– 0.55	8.79– 1.44	21.6– 3.18
	f	0.68	0.79– 0.21	1.27– 0.29	8.19– 1.08	20.1– 2.38
	g	1.34	0.34– 0.12	0.63– 0.19	8.13– 0.85	20.9– 1.87
	h	0.41	0.08– 0.02	0.16– 0.03	3.07– 0.20	7.78– 0.43
L_{XUV} cst	b	0.85	28.1– 9.30	75.0– 24.8
	c	1.38	14.8– 4.69	39.4– 12.5
	d	0.41	1.31– 0.19	...	8.70– 1.26	23.2– 3.37
	e	0.62	0.51– 0.07	1.23– 0.17	7.63– 1.03	20.4– 2.76
	f	0.68	0.23– 0.02	0.50– 0.05	7.12– 0.77	19.0– 2.06
	g	1.34	0.14– 0.01	0.32– 0.03	7.62– 0.61	20.3– 1.62
	h	0.41	0.02– <0.01	0.05– <0.01	2.82– 0.14	7.52– 0.37

Note. The two values given for each column correspond to the quantity of hydrogen lost (calculated for the nominal estimate of the XUV luminosity in Table 4 and the nominal masses) and the quantity of hydrogen available from photolysis (in bold, assuming an efficiency of 20%).

5.2.1. Outgassing from a Magma Ocean

At the early stages of planet evolution, magma oceans can outgas large fractions of water. The amount of outgassed water can range from less than 1% to 20% of a terrestrial-like planet mass based on typical compositions (see Elkins-Tanton & Seager 2008). For the Earth ($M_{\text{Earth}} = 5.972 \times 10^{24}$ kg), this would correspond to up to 800 oceans of water assuming chondritic CI meteorites as the planet’s building blocks. This number is clearly an upper limit, considering the fact that the Earth (and possibly the planets in the TRAPPIST-1 system) might have formed from much drier (intermediate size) planetary bodies or lost significant amounts of water in the impact-driven formation processes. Furthermore, the model of Hamano et al. (2013) suggests that planets with steam atmospheres at orbits with a stellar influx larger than about 300 W m^{-2} (the Earth’s current incoming solar radiation) would have much longer magma ocean phases and could hence possibly outgas much more of their initial water at an early stage in the first few 10–100 Myr, and thus end up much drier than planets at greater distances from their host star. Based on the heat fluxes for the TRAPPIST-1 planets today (see Gillon et al. 2017), planets b–d would fall in orbits with such elevated heat fluxes. However, at this point in time, it is almost impossible to estimate the initial water inventory after the planet formation phase (including magma ocean and a possible later delivery of water), because of a lack of detailed understanding of what the early radiation environment of TRAPPIST-1 looked like, whether the planets migrated inward from a greater distance during this epoch (at subcritical lower stellar flux levels), whether any of the planets had a steam atmosphere (hydrogen- and methane-rich atmospheres would have no outgoing radiation limit to slow cooling, see Elkins-Tanton 2013; and hence not fall under the Hamano et al. 2013 dichotomy), and whether any water was delivered by impactors after the magma ocean phase. Therefore, what we can constrain now are the limits to the outgassed amount of water during the magma ocean phase and the later maximum subsolidus outgassing of water assuming plausible ranges of post-

magma-ocean water content in the planet’s mantles (see next sections).

5.2.2. Outgassing after the Magma Ocean Phase

After the magma ocean phase, rocky planets cool mainly through subsolidus convection and outgas water through volcanism. Volcanic activity and outgassing are driven by the formation and transport of melt within the planet’s subsurface, which depend on the thermal profile, the melting temperature of rock, and on the advective transport of rock parcels within a planet’s lithosphere.

5.2.3. Methods

Melt is formed only where the temperature exceeds the melting temperature of rock. We, therefore, have to (1) model the interior depth-dependent thermal evolution of a planet and (2) know the melting curve of mantle rock in order to assess a planet’s ability to generate melt.

1. The thermal histories of planets are computed with an extended 1D boundary layer model (Stamenković et al. 2012), which agrees well with spherical 2D thermal evolution models (i.e., Hüttig & Stemmer 2008). The thermal evolution is described by two thermal boundary layers, which drive thermal convection and are used to parameterize the heat flux out of the core and out of the convective mantle, which is fed by secular cooling and radiogenic heat sources decaying in time. For simplicity, we assume the Earth’s radiogenic heat content to obtain a first insight into the TRAPPIST-1 planets; we do not expect our conclusions to significantly vary for alternative values based on some first tests.

We try to mimic an initially fully molten mantle by fitting the initial upper mantle temperature $T_m(0)$ to the solidus temperature of peridotite, $T_{\text{melt, peridotite}}$ (see below). For the highest initial core–mantle boundary temperature, $T_c(0)$, we use the melting temperatures of MgSiO_3 perovskite from Stamenković et al. (2011). This assumption allows us to fluently connect to an initial

early magma ocean stage. All scaling relations and parameters can be found in Stamenković et al. (2012).

- Our melt model has been described in detail in Stamenković & Breuer (2014) and for the melting temperature in the upper mantle (where the melt that drives outgassing is produced) our model uses the solidus for Earth-like peridotite, $T_{\text{melt, peridotite}}$. This $T_{\text{melt, peridotite}}$ is obtained by fitting the data from Herzberg et al. (2000), Zerr et al. (1998), and Fiquet et al. (2010; see Equation (7) in Stamenković & Breuer 2014).

Water can have a significant effect on reducing the solidus temperature of mantle rock (e.g., Asimow et al. 2004; Aubaud et al. 2004; Hirschmann 2006; Grove et al. 2009). Asimow et al. (2004) compute melting curves for water-undersaturated and water-saturated peridotite. Their water-saturated melting curve is close to a prediction based on the homologous temperature approach (for details, see, e.g., Katayama & Karato 2008; Stamenković et al. 2011). In the homologous temperature model, the melting temperature change corresponds to the enthalpy change of diffusion creep, E^* (at smaller pressures this approximately corresponds to the activation energy change), so that $T_{\text{melt, dry}}/T_{\text{melt, wet}} = E_{\text{dry}}^*/E_{\text{wet}}^*$. This corresponds to a melting point reduction of $\sim 20\%$ due to water saturation when we use the model of Karato & Wu (1993) for activation energies of dry and wet olivine. We, therefore, use our melting curve based on the water-saturated homologous temperature as the reference melting curve for water-saturated upper mantle rock.

The upper mantle water concentrations are thought to generally be below water saturation levels, typically between 50 and 200 ppm (partially up to 1000 ppm, still not saturated; Aubaud et al. 2004; Hirschmann 2006), at subduction zones locally oversaturated (e.g., Grove et al. 2009), and plumes are found to contain about 300–1000 ppm of water (Hirschmann 2006 for review). The storage capacity of olivine, on the other hand, has been estimated to increase with depth from ~ 25 ppm at 10 km to ~ 1300 ppm at 410 km for the Earth, strongly varying with water fugacity and hence temperature and depth. It is, however, possible that this value is about ~ 3 – 3.5 times too small, leading to more than ~ 0.4 weight % of water for mantle rock (see Hirschmann 2006 and references therein). On the other hand, based on geochemical constraints on $\text{K}_2\text{O}/\text{H}_2\text{O}$ ratios in basalts (Hirschmann 2006 for review), the bulk water content is estimated to be between 500 and 1900 ppm. For our first order of magnitude estimate for the TRAPPIST-1 system, we assume no depth dependence of water content or storage capability and use average bulk values of 500 ppm (minimal value bulk mantle) to 0.4% (upper saturation value) for mantle rock. The rheology is fixed to a Newtonian-type viscosity for a wet bulk mantle based on Karato & Wu (1993).

We vary the pressure dependence (activation volume V^*) of the mantle viscosity, from $V^* = 0$ to values calculated in Stamenković et al. (2011). We propagate this uncertainty in mantle viscosity throughout all calculations. Furthermore, we follow the probabilistic approach of Stamenković & Seager (2016), where we also propagate an uncertainty in our heat flux (Nusselt) scaling parameter β , allowing it to vary between 0.2 and $1/3$. By accounting for as many uncertainties as possible, we make sure that our results are as robust as possible. Within this parameter

space, we highlight a favored model with a value of $\beta \sim 0.3$ for the Nusselt–Rayleigh parameter and a pressure-dependent activation volume as computed in Stamenković et al. (2011), suggesting that this standard model best represents the thermal evolution of rocky planets of variable core size between 0.1 and 2 Earth masses, representative of the possible refractory planet masses for the TRAPPIST-1 planets. We fix the surface temperature to 298 K, as surface temperature variations found in the TRAPPIST-1 system today have no significant impact on our results (unless surface temperatures are above ~ 500 – 700 K).

Knowing a planet’s ability to generate melt at depth and in time is, however, not sufficient to calculate whether that parcel of melt can be brought to the surface, leading to potential outgassing. The latter depends strongly on two factors: (1) the density crossover pressure of mantle rock and (2) the tectonic mode of a planet.

- Melt generated at depth will rise to the surface as long as the density of the melt is smaller than that of the surrounding solid rock. However, on the Earth, typical mantle rock at pressures above 12 GPa does not rise to the surface, due to the density crossover, where melt becomes denser than surrounding solid rock (Ohtani et al. 1995). We note that this pressure value of 12 GPa varies with rock composition and especially water content (Jing & ichiro Karato 2009). Hence, we use the terrestrial value only as a reference point to explore whether the density crossover pressure might affect outgassing on the TRAPPIST-1 planets. Moreover, we do not account for any other mechanisms that could cause intrusive volcanism.
- The tectonic mode has two end members: plate tectonics (PT), as found on the Earth, and stagnant lid (SL) convection, as found on modern-day Mars. In the following, we will model outgassing for stagnant lid planets. Modeling outgassing in the plate tectonics mode is too sensitive to planet properties that we do not yet know from the TRAPPIST-1 planets, and hence we leave this to future work and refer to Schaefer & Sasselov (2015) for a more detailed discussion on outgassing on plate tectonics worlds.

For the TRAPPIST-1 planets, the uncertainties in mass are yet too large to infer much structural or compositional detail. What we can do now is model the thermal evolution, melt generation, and water outgassing assuming a terrestrial (refractory) planetary body with a mass between 0.1 and 2 Earth masses with variable iron core sizes from 0% to 65% (corresponding to coreless to Mercury-structured) in the stagnant lid mode—and put the TRAPPIST-1 planets in context with these results. Also, we note that we do not include tidal heating. To make significant conclusions about the effects of tidal heating on the thermal evolution of the TRAPPIST-1 planets, we need much better constraints on planet masses, their volatile content, and their structures. Therefore, better constraints on planet masses will significantly improve our predictions in the near future.

5.2.4. Results

We find that after the magma ocean phase, the TRAPPIST-1 planets can outgas significant amounts of water, especially the more massive ones. We show in Figure 13—while accounting for significant uncertainties in structure and model parameters

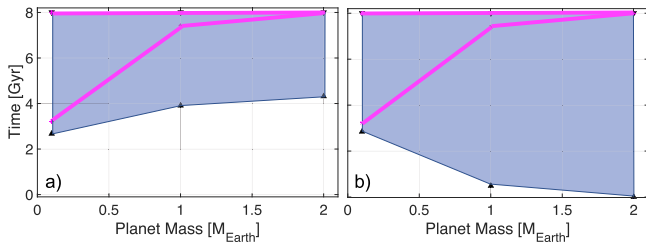


Figure 13. Duration of outgassing: As a function of refractory planet mass, we show the minimal duration of outgassing without (a) and with (b) consideration of an Earth-like reference density crossover, including all uncertainties specified in the methods (Section 5.2.3) in the blue shaded area. This uncertainty range is reduced to the domain between the pink lines when considering only our standard model. When the density crossover is considered, more massive planets can lack any extrusive volcanism, due to the melt source region being too deep (and hence at too high pressures). However, for our standard model, we find that for all cases, more massive planets can outgas longer.

—the range of minimal planet ages where outgassing can occur as a function of planet mass, assuming that the system is not older than 8 Gyr. Within this domain, we also plot the solution for our standard model (in pink) without and with consideration of the density crossover at 12 GPa. We see in Figure 13 that the minimal ages during which outgassing can occur vary largely (mainly modulated by core fraction and Nusselt-Rayleigh parameter uncertainty). However, our standard model shows a robust behavior, independent of density crossover, suggesting that planets formed from more massive refractory parent bodies will be able to outgas much longer. Figure 14 (showing the outgassed amount of water, in Earth oceans, for 500 ppm and 0.4 weight % of water, respectively) also exemplifies that planets with more massive refractory parent bodies can outgas more water and outgas that water at much later times in their evolution.

Combining this finding with Figure 9, which shows that planets within the orbits of TRAPPIST-1d and TRAPPIST-1h enter the HZ within about 100 Myr to a few hundred million years, and considering that the largest atmospheric loss processes occur before entering the HZ, suggest that especially planets farther away from TRAPPIST-1 and planets that are more massive could deliver up to one or two ocean masses of water after they entered the HZ. This emphasizes that late-stage geophysical outgassing might be a critical component helping to sustain habitable environments within the TRAPPIST-1 system.

6. Discussion

We observed the $\text{Ly}\alpha$ line of TRAPPIST-1 with *HST*/STIS in 2016 December, at the time of planet c transiting. When compared with previous observations obtained in 2016 September and November, this new measurement revealed that the stellar line evolved significantly in the last visit. It shows an increased emission with broader wings, which might trace an increase in the temperature of the stellar chromosphere. The relation from Youngblood et al. (2016) between the stellar rotation period and $\text{Ly}\alpha$ surface flux of early-type M dwarfs predicts significantly stronger $\text{Ly}\alpha$ emission than we detected for TRAPPIST-1. Our measured $\text{Ly}\alpha$ fluxes would correspond to rotation periods of ~ 84 days (based on Visits 1–3 $\text{Ly}\alpha$ flux) and ~ 54 days (based on Visit 4 $\text{Ly}\alpha$ flux), whereas the rotation period from K2 photometric data is ~ 3.3 days (Luger et al. 2017). This is in contrast to our detection of N V emission, which we find to be consistent with the previously measured

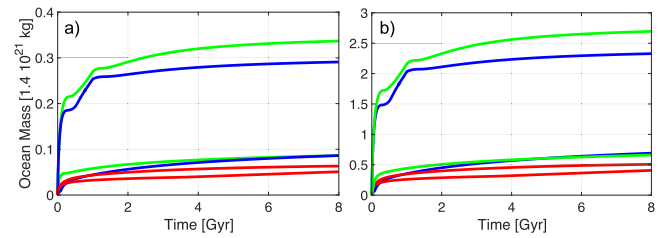


Figure 14. Outgassed water: We plot the range for the amount of outgassed water as a function of planet age for planets of refractory planet mass $M = 0.1$ (red), 1 (blue), and 2 (green). The two colored lines delimit in each case the range of uncertainties in planet structure (from coreless to Mercury-structured) for our standard model. Figure (a) assumes 500 ppm of water in the planet's mantle and (b) saturation levels of 0.4 weight %.

X-ray flux. Together these observations support our hypothesis that TRAPPIST-1 has a weak chromosphere compared to its transition region and corona (Wheatley et al. 2017, B17).

The spectra in 2016 December are subjected to a strong air glow contamination, which could have biased the extraction of the TRAPPIST-1 $\text{Ly}\alpha$ line. Nonetheless, a careful analysis of the stellar line shape tentatively suggests an absorption from neutral hydrogen at high velocity in the blue wing. This signature does not seem to correlate with the transit of TRAPPIST-1c, but could originate from a system-wide neutral hydrogen cloud sustained by the evaporation of several planets and shaped by the very low radiation pressure and photoionization from TRAPPIST-1. Alternatively, the peculiar shape of the TRAPPIST-1 $\text{Ly}\alpha$ line in this epoch could result from physical mechanisms specific to or magnified in ultracool dwarfs. In any case, the long-term and possibly short-term variability in the intrinsic $\text{Ly}\alpha$ line of TRAPPIST-1 prevents us from constraining the presence of a putative hydrogen exosphere around planet c, and it calls for an ongoing monitoring of the star both outside and during all planet transits.

Combining all measurements of TRAPPIST-1 $\text{Ly}\alpha$ and X-ray emissions, we estimated the present-day XUV irradiation of the planets. Using simple assumptions on the evolution of the irradiation over time, we calculated the history of hydrodynamic water loss from the planets in the energy-limited regime. With our current knowledge of the TRAPPIST-1 system, the major uncertainty on the water loss estimates comes from the uncertainty on the planet masses, rather than on the XUV luminosity. Setting the masses to their nominal estimates from Gillon et al. (2017), we found that planet g and those closer in could have lost more than 20 Earth oceans through hydrodynamic escape, if the system is as old as 8 Gyr. Planets b, c, and possibly d could still be in a runaway phase, but if water loss drops down significantly within and beyond the HZ, planets e, f, g, and h might have lost less than three Earth oceans. We caution that our water loss estimates were derived in a simplified framework and should be considered as upper limits because our assumptions likely maximize the XUV-driven escape. We refer the reader to Section 6 of Bolmont et al. (2017) for more details about these limitations. Furthermore, we found that photodissociation of water in the upper atmospheres of the TRAPPIST-1 planets is likely to be the limiting process, as hydrogen is produced at a lower rate than it is lost through hydrodynamic escape. The photolysis efficiency is expected to be lower than about 20%, in which case all planets but TRAPPIST-1b and c could still harbor significant amounts of water. Naturally this also depends on the age of the system and whether the planets formed with a small

water content (as suggested by planetary formation models; Ormel et al. 2017) or as planet oceans (as hinted by the low densities of the outer planets, especially TRAPPIST-1f; Gillon et al. 2017; Wang et al. 2017). We have also shown that late-stage outgassing could contribute significant amounts of water after the planets have entered the HZ. The amount of water outgassed after a few hundred million years (after which TRAPPIST-1h to e, and possibly d, have entered the HZ) is greater for planets with more massive refractory parent bodies. Improving our constraints on the planet masses of the TRAPPIST-1 system will therefore significantly improve our understanding of the variable outgassing capabilities of the TRAPPIST-1 planets and hence the current state of their atmospheres.





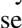

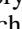



Our study focused on hydrodynamic water loss driven by the quiescent stellar XUV irradiation. We also investigated the effects of photolysis and outgassing, but we did not account for other physical mechanisms competing between the erosion of the atmospheres and their replenishing. For example, the presence of other gases in the atmosphere would act to slow down the hydrodynamic outflow (just as in our model the oxygen atoms can exert a drag on the hydrogen flow), although the background atmosphere could also be exposed to evaporation. We refer the reader to Section 5 of Ribas et al. (2016) for an extensive discussion about the loss of the background atmosphere and other escape processes. Stellar flares could occasionally increase the energy input into the atmospheres, enhancing the escape rate. However, no flaring activity was observed in TRAPPIST-1 X-ray and FUV observations, and the flares detected in optical (Luger et al. 2017; Vida et al. 2017) and infrared (Gillon et al. 2016, 2017) wavelengths point toward a low activity, with weak flares once every few days and stronger flares once every two to three months. The planetary atmospheres might also have been eroded by the stellar wind of TRAPPIST-1, especially when it was more active during the early phases of the system. Assuming that the planets are unmagnetized, Dong et al. (2017) derived upper limits on the atmospheric ion escape driven by the stellar wind. Tidal heating (due to the planet's proximity to the star and the mutual dynamical interactions maintaining their slightly eccentric orbits) could maintain significant magnetospheres, able to protect the planets from a putative stellar wind, or it could suppress dynamo activity. Furthermore, planetary magnetic fields can, depending on the specific interaction between planet and star, enhance or reduce atmospheric loss rates (e.g., Strangeway et al. 2005). Currently we have no constraints on the ability of the TRAPPIST-1 planets to generate magnetic fields, as this significantly depends on planet composition and structure. We also lack knowledge about the winds of ultracool dwarfs and their evolution with the stellar magnetic field over time, although TRAPPIST-1 is so cold that its atmosphere likely has a low level of ionization, resulting in a lower emission of charged particles than for a hotter star like Proxima Centauri (e.g., Mohanty et al. 2002).

Understanding the nature of the TRAPPIST-1 planets and their potential habitability will thus require the combination of theoretical studies (to better understand the time-dependent processes leading to geophysically driven water outgassing, the atmospheric loss processes, and the role of magnetic fields in affecting them) with further photometric observations (to refine the planet radii and more importantly their masses through TTV), X-ray and UV observations of the stellar spectrum (to

monitor the activity of the star and measure the high-energy irradiation of the planetary atmospheres, currently poorly known; O'Malley-James & Kaltenegger 2017), and transit spectroscopy in the FUV (to detect escaping hydrogen and possibly oxygen) and in the IR (to search for the signature of water in the bottom atmospheric layers).

We give our thanks to the referee for a detailed review and useful suggestions. We thank A. Lecavelier Des Etangs for insightful discussion about habitability and extraction of the STIS spectra. We thank S. Raymond, F. Selsis, and H. Wakeford for helpful comments about this study. This work is based on observations made with the NASA/ESA *Hubble Space Telescope*, obtained at the Space Telescope Science Institute, which is operated by the Association of Universities for Research in Astronomy, Inc., under NASA contract NAS 5-26555. This work has been carried out partly in the frame of the National Centre for Competence in Research "PlanetS" supported by the Swiss National Science Foundation (SNSF). This project has received funding from the European Research Council (ERC) under the European Union's Horizon 2020 research and innovation program (project FOUR ACES; grant agreement No. 724427). V.B. acknowledges the financial support of the SNSF. V.S. has received support from the Simons Collaboration on the Origins of Life (338555, VS). P. W. is supported by STFC consolidated grant ST/P000495/1. M. Gillon, E. Jehin, and V. Van Grootel are Belgian F.R.S.-FNRS Research Associates. This work was partially supported by a grant from the Simons Foundation (PI Queloz, grant number 327127). L.D. acknowledges support from the Gruber Foundation Fellowship.

ORCID iDs

V. Bourrier  <https://orcid.org/0000-0002-9148-034X>
 J. de Wit  <https://orcid.org/0000-0003-2415-2191>
 V. Stamenković  <https://orcid.org/0000-0003-2416-3683>
 P. J. Wheatley  <https://orcid.org/0000-0003-1452-2240>
 A. J. Burgasser  <https://orcid.org/0000-0002-6523-9536>
 B.-O. Demory  <https://orcid.org/0000-0002-9355-5165>
 D. Ehrenreich  <https://orcid.org/0000-0001-9704-5405>
 M. Gillon  <https://orcid.org/0000-0003-1462-7739>
 N. Lewis  <https://orcid.org/0000-0002-8507-1304>
 A. H. M. J. Triaud  <https://orcid.org/0000-0002-5510-8751>

References

- Asimow, P. D., Dixon, J. E., & Langmuir, C. H. 2004, *GGG*, 5, Q01E16
- Aubaud, C., Hauri, E. H., & Hirschmann, M. M. 2004, *GeoRL*, 31, L20611
- Baraffe, I., Homeier, D., Allard, F., & Chabrier, G. 2015, *A&A*, 577, A42
- Barnes, R., Deitrick, R., Luger, R., et al. 2016, arXiv:1608.06919
- Barnes, R., & Heller, R. 2013, *AsBio*, 13, 279
- Bolmont, E., Selsis, F., Owen, J. E., et al. 2017, *MNRAS*, 464, 3728
- Bourrier, V., Ehrenreich, D., King, G., et al. 2016a, *A&A*, 597, A26
- Bourrier, V., Ehrenreich, D., & Lecavelier des Etangs, A. 2015, *A&A*, 582, A65
- Bourrier, V., Ehrenreich, D., Wheatley, P. J., et al. 2017, *A&A*, 599, L3
- Bourrier, V., & Lecavelier des Etangs, A. 2013, *A&A*, 557, A124
- Bourrier, V., Lecavelier des Etangs, A., Dupuy, H., et al. 2013, *A&A*, 551, A63
- Bourrier, V., Lecavelier des Etangs, A., Ehrenreich, D., Tanaka, Y. A., & Vidotto, A. A. 2016b, *A&A*, 591, A121
- Burgasser, A. J., & Mamajek, E. E. 2017, *ApJ*, submitted, arXiv:1706.02018
- Chabrier, G., Gallardo, J., & Baraffe, I. 2007, *A&A*, 472, L17
- Crossfield, I. J. M., Knutson, H., Fortney, J., et al. 2012, *ApJ*, 752, 81
- de Wit, J., Wakeford, H. R., Gillon, M., et al. 2016, *Natur*, 537, 69
- Dong, C., Jin, M., Lingam, M., et al. 2017, arXiv:1705.05535

- Dupuy, T. J., & Liu, M. C. 2017, *ApJS*, **231**, 15
- Ehrenreich, D., Bourrier, V., Bonfils, X., et al. 2012, *A&A*, **547**, A18
- Ehrenreich, D., Bourrier, V., Wheatley, P. J., et al. 2015, *Natur*, **522**, 459
- Ekenbäck, A., Holmström, M., Wurz, P., et al. 2010, *ApJ*, **709**, 670
- Elkins-Tanton, L. T. 2013, *Natur*, **497**, 570
- Elkins-Tanton, L. T., & Seager, S. 2008, *ApJ*, **685**, 1237
- Erkaev, N. V., Kulikov, Y. N., Lammer, H., et al. 2007, *A&A*, **472**, 329
- Filippazzo, J. C., Rice, E. L., Faherty, J., et al. 2015, *ApJ*, **810**, 158
- Fiquet, G., Auzende, A. L., Siebert, J., et al. 2010, *Sci*, **329**, 1516
- France, K., Froning, C. S., Linsky, J. L., et al. 2013, *ApJ*, **763**, 149
- France, K., Parke Loyd, R. O., Youngblood, A., et al. 2016, *ApJ*, **820**, 89
- Gillon, M., Jehin, E., Lederer, S. M., et al. 2016, *Natur*, **533**, 221
- Gillon, M., Triaud, A. H. M. J., Demory, B.-O., et al. 2017, *Natur*, **542**, 456
- Grove, T. L., Till, C. B., Lev, E., Chatterjee, N., & Médard, E. 2009, *Natur*, **459**, 694
- Guinan, E. F., Engle, S. G., & Durbin, A. 2016, *ApJ*, **821**, 81
- Hamano, K., Abe, Y., & Genda, H. 2013, *Natur*, **497**, 607
- Heays, A. N., Bosman, A. D., & van Dishoeck, E. F. 2017, *A&A*, **602**, A105
- Herzberg, C., Rateron, P., & Zhang, J. 2000, *GGG*, **1**, 1051
- Hirschmann, M. M. 2006, *AREPS*, **34**, 629
- Holman, M. J., & Murray, N. W. 2005, *Sci*, **307**, 1288
- Holmström, M., Ekenbäck, A., Selsis, F., et al. 2008, *Natur*, **451**, 970
- Hunten, D. M., Pepin, R. O., & Walker, J. C. G. 1987, *Icar*, **69**, 532
- Hüttig, C., & Stemmer, K. 2008, *PEPI*, **171**, 137
- Jing, Z., & ichiro Karato, S. 2009, *ChGeo*, **262**, 100
- Joshi, M. M., & Haberle, R. M. 2012, *AsBio*, **12**, 3
- Jura, M. 2004, *ApJL*, **605**, L65
- Kaltenegger, L., & Traub, W. A. 2009, *ApJ*, **698**, 519
- Karato, S.-I., & Wu, P. 1993, *Sci*, **260**, 771
- Katayama, I., & Karato, S.-I. 2008, *PEPI*, **166**, 57
- Kopparapu, R. K. 2013, *ApJL*, **767**, L8
- Koskinen, T. T., Aylward, A. D., & Miller, S. 2007, *Natur*, **450**, 845
- Kulow, J. R., France, K., Linsky, J., & Loyd, R. O. P. 2014, *ApJ*, **786**, 132
- Lammer, H., Selsis, F., Ribas, I., et al. 2003, *ApJL*, **598**, L121
- Lecavelier des Etangs, A. 2007, *A&A*, **461**, 1185
- Lecavelier des Etangs, A., Bourrier, V., Wheatley, P. J., et al. 2012, *A&A*, **543**, L4
- Lecavelier des Etangs, A., Ehrenreich, D., Vidal-Madjar, A., et al. 2010, *A&A*, **514**, A72
- Leconte, J., Forget, F., & Lammer, H. 2015, *ExA*, **40**, 449
- Léger, A., Selsis, F., Sotin, C., et al. 2004, *Icar*, **169**, 499
- Linsky, J. L., Fontenla, J., & France, K. 2014, *ApJ*, **780**, 61
- Luger, R., & Barnes, R. 2015, *AsBio*, **15**, 119
- Luger, R., Sestovic, M., Kruse, E., et al. 2017, *NatAs*, **1**, 0129
- Miguel, Y., Kaltenegger, L., Linsky, J. L., & Rugheimer, S. 2015, *MNRAS*, **446**, 345
- Mohanty, S., Basri, G., Shu, F., Allard, F., & Chabrier, G. 2002, *ApJ*, **571**, 469
- Ohtani, E., Nagata, Y., Suzuki, A., & Kato, T. 1995, *ChGeo*, **120**, 207
- O'Malley-James, J. T., & Kaltenegger, L. 2017, *MNRAS*, **469**, L26
- Ormel, C., Liu, B., & Schoonenberg, D. 2017, *A&A*, **604**, A1
- Owen, J. E., & Alvarez, M. A. 2016, *ApJ*, **816**, 34
- Parenti, S. 2014, *LRSP*, **11**, 1
- Pascucci, I., Apai, D., Luhman, K., et al. 2009, *ApJ*, **696**, 143
- Pecaut, M. J., & Mamajek, E. E. 2016, *MNRAS*, **461**, 794
- Pfalzner, S., Steinhausen, M., & Menten, K. 2014, *ApJL*, **793**, L34
- Quarles, B., Quintana, E. V., Lopez, E. D., Schlieder, J. E., & Barclay, T. 2017, *ApJL*, **842**, L5
- Ranjan, S., Wordsworth, R. D., & Sasselov, D. D. 2017, *ApJ*, **843**, 110
- Ribas, I., Bolmont, E., Selsis, F., et al. 2016, *A&A*, **596**, A111
- Schaefer, L., & Sasselov, D. 2015, *ApJ*, **801**, 40
- Schrijver, C. J., Elmore, C., Kliem, B., Török, T., & Title, A. M. 2008, *ApJ*, **674**, 586
- Scuflaire, R., Théado, S., Montalbán, J., et al. 2008, *Ap&SS*, **316**, 83
- Seager, S., & Sasselov, D. D. 2000, *ApJ*, **537**, 916
- Selsis, F., Chazelas, B., Bordé, P., et al. 2007, *Icar*, **191**, 453
- Solomatov, V. 2007, in *Treatise on Geophysics*, ed. G. Schubert (Amsterdam: Elsevier), 91
- Stamenković, V., & Breuer, D. 2014, *Icar*, **234**, 174
- Stamenković, V., Breuer, D., & Spohn, T. 2011, *Icar*, **216**, 572
- Stamenković, V., Noack, L., Breuer, D., & Spohn, T. 2012, *ApJ*, **748**, 41
- Stamenković, V., & Seager, S. 2016, *ApJ*, **825**, 78
- Strangeway, R. J., Ergun, R. E., Su, Y.-J., Carlson, C. W., & Elphic, R. C. 2005, *JGRA*, **110**, A03221
- Tamayo, D., Rein, H., Petrovich, C., & Murray, N. 2017, *ApJL*, **840**, L19
- Turbet, M., Leconte, J., Selsis, F., et al. 2016, *A&A*, **596**, A112
- Vida, K., Kővári, Z., Pál, A., Oláh, K., & Kriskovics, L. 2017, *ApJ*, **841**, 124
- Vidal-Madjar, A., Lecavelier des Etangs, A., Désert, J.-M., et al. 2003, *Natur*, **422**, 143
- Wang, S., Wu, D.-H., Barclay, T., & Laughlin, G. P. 2017, *ApJ*, submitted, arXiv:1704.04290
- Wheatley, P. J., Loudon, T., Bourrier, V., Ehrenreich, D., & Gillon, M. 2017, *MNRAS*, **465**, L74
- Winn, J. N. 2010, arXiv:1001.2010
- Wordsworth, R., & Pierrehumbert, R. 2014, *ApJL*, **785**, L20
- Yang, J., Cowan, N. B., & Abbot, D. S. 2013, *ApJL*, **771**, L45
- Youngblood, A., France, K., Parke Loyd, R. O., et al. 2016, *ApJ*, **824**, 101
- Zerr, A., Diegeler, A., & Boehler, R. 1998, *Sci*, **281**, 243